On an Instrument for the Coherent Investigation of Nitrogen-Vacancy Centres in Diamond

by

Om Patange

A thesis
presented to the University of Waterloo
in fulfillment of the
thesis requirement for the degree of
Master of Science
in
Physics

Waterloo, Ontario, Canada, 2013

I hereby declare that I am the sole author of this thesis. This is a true copy of the thesis, including any required final revisions, as accepted by my examiners.

I understand that my thesis may be made electronically available to the public.

Abstract

It is my hope that this thesis may serve as a guide for future students wishing to build a microscope from scratch. The design and construction of a scanning, confocal fluorescence microscope equipped with shaped microwave excitation is detailed. The use of the microscope is demonstrated by coherently manipulating single Nitrogen-Vacancy centres in diamond. Further the instrument is used to investigate a dual Halbach array magnet system.

Acknowledgements

There are many people I wish to thank. Firstly, I thank Professor David Cory for seeing in me some spark of a scientist and hiring me in his fledgling Waterloo lab. David has consistently invested his trust in me by giving me greater and greater responsibilities and has challenged me to work to my full potential. His influence on my thinking and confidence is indelible.

I cannot thank Ian Hincks enough for tutoring me in the ways of quantum information for the duration of this degree. From answering my first question on the orthogonality of vectors on the Bloch sphere to working together on studying NV centres, Ian has been of immeasurable support.

I would like to thank the 'NV Group' for many fruitful discussions and in particular Osama Mousa for making the 'NV Meetings' productive. I have also benefited greatly from working with Osama in the lab. Chris Granade has been a constant inspiration for me to be a better scientist. Working with Dusan Sarenac on the Halbach project was a fruitful experience. Being part of the broader Cory Group and indeed the Institute for Quantum Computing has been an enriching experience and I thank everyone involved for making it so. I thank the Waterloo Institute for Nanotechnology for granting me a WIN Nanofellowship to support my work.

In addition to working with NVs I had the fortune of working alongside the one, and only, Patryk Gumann. With Pat I got a glimpse of the world of low-temperature physics as well as an education in how to be human.

Most importantly I thank my family who have given me tremendous support over the years and have shown great tolerance of my odd working habits and negligence of filial responsibilities.

Dedication

To the process of doing science.

Table of Contents

List of Tables

List of Figures

Chapter 1

Introduction

The field of Quantum Information has matured: with a robust theoretical vision of how quantum devices [1, 2] and computers [3] could be used, what is needed to produce them in the lab [4, 5], and key proof-of-concept experiments performed [6, 7]. The current scope of the field is largely to explore a variety of potential experimental systems that might be suitable to build robust quantum bits (qubits). Some possibilities are superconducting devices [8, 9], quandum dots [10], molecular films hosting electron and nuclear spins [11], and solid-state defects such as Nitrogen-Vacancy (NV) centres in diamond [12].

NV centres have many appealing characteristics. Most importantly, NVs have been shown to have coherence times of milliseconds at room temperature [13, 14] and approaching a second at low temperature [15]. That they are defects in the solid-state and one NV at a time can be controlled and measured makes NVs promising for scaled-up demonstration of quantum information processors. Demonstrations of long lived quantum registers constructed out of nuclear spins in the NV's environment [16, 17] and two-NV entanglement lend support to this promise [18, 19].

In the immediate future NVs are fruitful systems for the construction of quantum sensors. The sensing of a single electron spin external to the NV's host diamond has been reported [20]. Magnetic vector fields have also been measured with arrays of NVs [21]. Various applications of NV sensors to biological samples have also been demonstrated. Magnetotactic bacteria have been observed using arrays of NVs [22]. The local temperature inside living cells was probed using NVs in nanodiamonds [23]. Nanodiamonds were also proposed as a tool to investigate the action of ion channels in cells [24] and experimental work in this direction was recently reported [25].

A challenge for making novel NV-based devices is the fabrication of micro- and nano-

structures in diamond. High quality NVs can now routinely be fabricated via nitrogen-implantation [26] as well as enriched Chemical Vapour Deposition [27]. Excellent progress has been made in making photonic structures hosting single NVs [28] and applying these structures for magnetic sensing [29].

In order to study this promising quantum object specialized instruments are needed. My thesis is on one such instrument, a confocal fluorescence microscope equipped with shaped microwave excitation that I built to conduct coherent investigations of single NV centres. In Chapter 2 I will first review the properties of the NV centre. Next, in Chapter 3, I will describe in detail the optical apparatus that is the confocal microscope. In Chapter 4 I will prove my thesis by demonstrating coherent control of single NVs. The investigation of a novel magnet array system performed with this microscope is presented next in Chapter 5. I will conclude in Chapter 6 by describing work under-way in the laboratory using this instrument and future work.

Chapter 2

Nitrogen-Vacancy Centres in Diamond

2.1 The Physical Defect

Diamond is a remarkable material holding the record for physical properties such as hardness and stiffness [30]. It has one of the highest indices of refraction at $n = 2.4$ and is transparent to a wide spectrum of electromagnetic radiation due to its large band gap at 5.45 eV [30]. It has captured the imagination of royalty [31] and become a central facet of modern marital proceedings. Its importance has motivated work to synthetically produce diamond, which started with High-Pressure High-Temperature experiments [32, 33]. Now diamond can be deposited out of vapour in a Plasma-Enhanced Chemical Vapour Deposition system [34], see inset of 2.1a. Extremely pure and crystalline diamonds can now be grown in the lab, with defect concentrations on the order of parts-per-billion [35].

However, even the best diamond has defects, some of which fluoresce. The Nitrogen-Vacancy centre is one such colour centre that has risen to prominence. In the diamond lattice a nitrogen atom is substituted for a carbon and adjacent to it a carbon atom is removed, forming a Nitrogen-Vacancy centre, see Figure 2.1a. Each of the three nearest-neighbour carbon atoms to the vacancy contributes a single dangling-bond electron to the NV and the nitrogen contributes two electrons as it has a valence of five. These five electrons comprise the neutral NV^0 centre, which has been studied only cursorily [36]. An extra electron produces the much studied negatively charged NV^- [37].
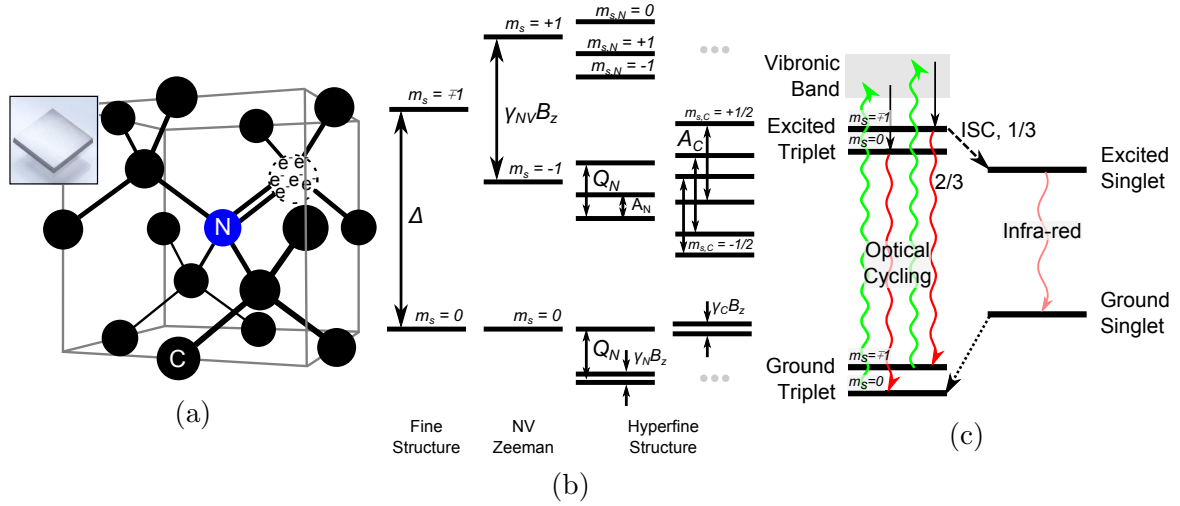
Figure 2.1: a) Within the diamond lattice a substitutional nitrogen and adjacent vacancy (dotted circle) form the Nitrogen-Vacancy centre. Also represented are three dangling bond electrons from the nearest neighbour carbons, two from the nitrogen and a sixth extra electron forming the negatively charged NV, image adapted from [38]. Inset: A typical diamond used in the present experiments, image from [35]. b) The electronic structure of the ground state of the NV, the energy level spacings are not to scale. The ellipses in place of ^{13}C levels are for clarity of presentation. The bottom ellipsis is in place for four energy levels that would be split by the carbon Zeeman terms and would stem from the two nitrogen Zeeman terms. The upper ellipsis is in place for a structure similar to the $m_s = -1$ carbon levels. c) The full electronic structure of the NV showing the optical and infra-red transitions, Inter-System Crossing (ISC) of the excited triplet to the excited singlet state, and the path of the ground singlet state to the $m_s = 0$ state of the ground triplet.

2.2 Electronic Structure of the Ground State

The symmetry of the negatively charged NV centre reduces the six electron system to an effective two electron, spin-1, system where the two electrons are exchange coupled [39]. Empirically the ground state of the NV centre is found to be in the triplet manifold of this interaction [39], see figure 2.1b. Further, a magnetic dipolar interaction between these two electrons lifts the triplet degeneracy by the so-called Zero-Field Splitting (ZFS) into the spin-quantum number $m_s = 0$ and $m_s = \pm 1$ levels, see Figure 2.1b [40, 41]. The ZFS is $\Delta \approx 2.87$ GHz, which corresponds to microwave frequencies. The $m_s = \pm 1$ degeneracy

can further be lifted by an external magnetic field, $\vec{B}$, via the Zeeman interaction, which is found to be nearly isotropic with a gyromagnetic ratio of $\gamma \approx 2.8$ MHz/G, [42]. The fine structure and Zeeman Hamiltonian of the NV is:

$$\frac{H_{NV}}{\hbar} = \Delta S_z^2 + \gamma \vec{S} \cdot \vec{B} \tag{2.1}$$

where the spin-1 operators are [43]:

$$S_x = \begin{pmatrix} 0 & 1 & 0 \\ 1 & 0 & 1 \\ 0 & 1 & 0 \end{pmatrix}, \quad S_y = \begin{pmatrix} 0 & -i & 0 \\ i & 0 & -i \\ 0 & i & 0 \end{pmatrix}, \quad S_z = \begin{pmatrix} 1 & 0 & 0 \\ 0 & 0 & 0 \\ 0 & 0 & -1 \end{pmatrix} \tag{2.2}$$

The NV exhibits hyperfine structure due to interaction with associated nuclear spins, see Table 2.1. The most abundant nitrogen isotope, ^{14}N, has a spin-1 nucleus. In addition to its hyperfine interaction with the NV it has a quadrupolar interaction [44]. Due to the scarcity of ^{15}N, it is typically encountered only in samples implanted with ^{15}N and we neglect it in this work. In principle there can be many ^{13}C nuclei coupled to a single NV, each contributing a hyperfine interaction with the NV. In practice, with diamonds made of natural abundance carbon most NVs have only one strongly coupled carbon. The Hamiltonian for the NV with nuclear spins is:

$$\frac{H_{NV,^{14}N,^{13}C}}{\hbar} = \Delta S_z^2 + \gamma \vec{S} \cdot \vec{B} + \vec{S} \cdot \mathbf{A}_N \cdot \vec{I}_N + \vec{I}_N \cdot \mathbf{Q} \cdot \vec{I}_N + \gamma_N \vec{I}_N \cdot \vec{B} + \sum_i \left(\vec{S} \cdot \mathbf{A}_{C,i} \cdot \vec{I}_{C,i} + \gamma_C \vec{B} \cdot \vec{I}_{C,i} \right) \tag{2.3}$$

where $\vec{I}_N$ is a vector of spin-1 operators for ^{14}N analogous to equations 2.2, $\vec{I}_{C,i}$ are vectors of spin-$^1/_2$ Pauli operators [43] for the ith ^{13}C in the diamond lattice, $\mathbf{A}_{N(C)}$ are hyperfine tensors between the NV and ^{14}N (^{13}C), and $\mathbf{Q}$ is the quadrupolar term of the ^{14}N.

Thus, applying microwave radiation at the appropriate frequencies allows for coherent manipulation of this effective spin-1 system and observation of nearby nuclear spins, see Chapter 4.

2.3 Optical Transitions and the Singlets

Applying optical radiation to the NV excites it from the triplet ground state to the triplet excited state [40], see Figure 2.1c. If the NV begins in the $m_s = 0$ level the result is a cycling transition, with an excited state lifetime of ~13 ns, leading to fluorescence in the

Nuclear Isotope	Abundance %	Spin	Hyperfine
nitrogen-14	>99	1	$Q = 5$ MHz, $A_{N,\parallel} = 2.3$ MHz, $A_{N,\perp} = 2.1$ MHz [44]
nitrogen-15	<1	$^1/_2$	$A_{N,\parallel} = 3.0$ MHz, $A_{N,\perp} = 3.6$ MHz [42]
carbon-12	99	0	-
carbon-13	1.1	$^1/_2$	Varies with position in lattice. Starts at $A_C \approx 130$ MHz [45, 46] and $A_C \approx 20$ kHz has been resolved [47]

Table 2.1: List of relevant nuclear isotopes in the NV system

optical regime. On the other hand, if the NV begins in the $m_s = \pm 1$ levels the same cycling transition happens ~2/3 of the time, while ~1/3 of the time the excited state undergoes an Inter-System Crossing (ISC) to the excited singlet state of the two-electron exchange interaction. This radiatively decays to the ground singlet state via an infra-red photon [48]. The singlet states have a combined lifetime of ~300 ns. Finally, the ground state singlet is preferentially pumped to the $m_s = 0$ level of the triplet ground state of the NV. Note, the excited state triplet has a Zero-Field Splitting of ~1.4 GHz [49, 50].

These optical transitions can be resolved spectroscopically at low-temperatures with wavelengths around ~637 nm for the triplet and ~1046 nm for the singlet, probing the so called Zero-Phonon Lines (ZPL) [51]. However, at room temperature these resonant transitions are widened by phonon-assisted processes and there exists a wide Phonon-assisted Side Band (PSB) of emission from ~637 to 800 nm, or red to near infra-red [52] for the triplet optical transition and between ~1046 to 1200 nm for the singlet, or near infra-red [48]. Similarly, the NVs can be excited with non-resonant green light at 532 nm [52].

Putting it all together, the $m_s = 0$ and $m_s = \pm 1$ levels of the NV ground state can be discerned optically due to the differential optical fluorescence occurring over the lifetime of the singlet state by a detector insensitive to mid-IR radiation. This will be exploited to investigate single NV centres with the technique of Optically Detected Magnetic Resonance described in Chapter 4 and the home-built confocal microscope detailed in Chapter 3.

The interested reader is directed to an excellent review on the known and debated

properties of NV centres that has recently been published [53].

Chapter 3

Confocal Microscope

The Nitrogen-Vacancy centres investigated in this work are typically located in bulk diamond samples. Despite being very pure crystals, these samples contain an abundance of NV defects. To detect and manipulate only one NV at a time a scanning laser, fluorescence, confocal microscope was built with the additional capability of shaped microwave excitation of the NV spin. The following describes the optical microscope in detail.

3.1 Introduction to Confocal Microscopy

Confocal microscopy relies on the concept of conjugate planes. If a point source is imaged by an optical system then the source plane and the image plane are termed conjugate planes [54]. The source (image) plane contains the point source (image point) and is perpendicular to the optical axis. Figure 3.1 illustrates the concept with an optical system consisting of two biconvex lenses.

The main feature of a confocal microscope is that it blocks the light from all but the point source of interest [55, 56]. This is accomplished by placing a pinhole in the image plane such that it intersects the image point of interest, see Figure 3.1. The confocal condition is the detection of a point source through a pinhole placed in this way and the pinhole and the point source are said to be confocal. Off-axis sources are imaged off-axis, but in the image plane and so are blocked by the pinhole. On-axis sources from other source planes are focused before or after the pinhole, reducing the intensity of light getting through the pinhole.
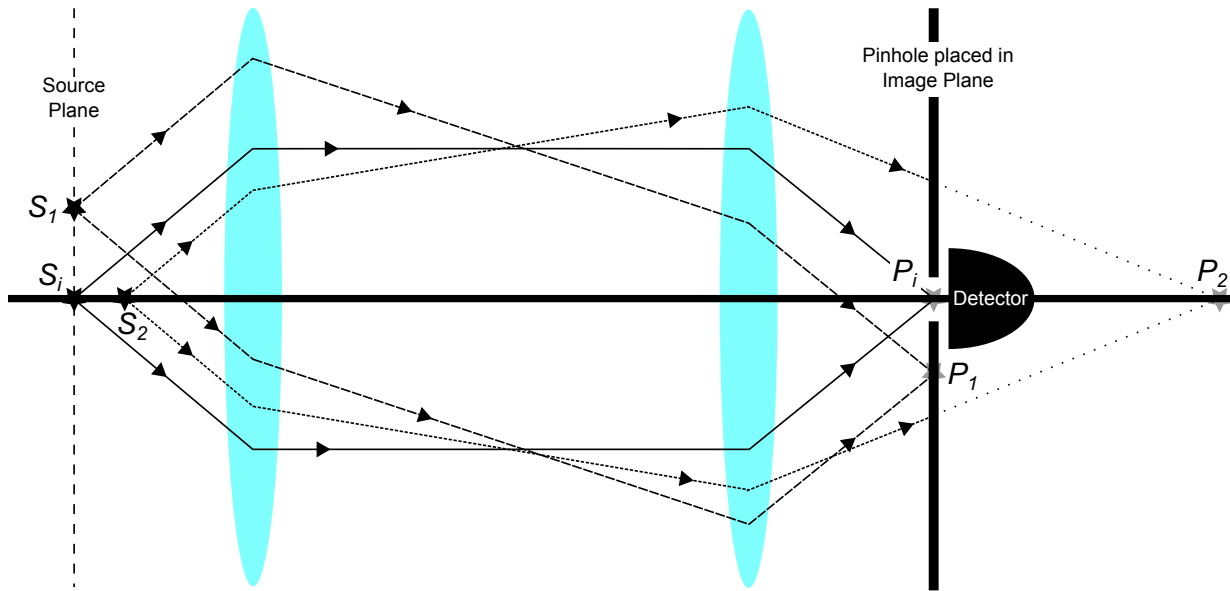
Figure 3.1: The principle of confocal microscopy. The source and image planes are conjugate planes, as illustrated for a simple optical system consisting of two biconvex lenses. Various point sources, S_x, and their conjugate image points, P_x, are shown. The pinhole blocks all but the light from the point source of interest, S_i.

A scanning confocal microscope allows access to more than one point source of interest. This can be accomplished in many ways. The sample containing the point source(s) can be moved such that the new point source of interest is brought to the confocal point. Alternatively, the pinhole can be scanned around such that the confocal spot is moved. A variation on these techniques is used in the physical implementation described in the next section.

3.2 Physical Implementation of Laser Scanning, Fluorescence, Confocal Microscope

The microscope can be divided into six main functional components: the source, switching arm, mode shaping arm, scanning optics, sample stage, and pinhole detector; see Figure 3.12.

9

Source

The source requirements for this microscope are minimal. The NV is excited with off-resonant green light, see Figure 2.1c. It is ideal for the spatial mode of the source to be a propagating beam in the TEM_{00} mode [54] for ease of implementation of the other components of the microscope, see Figure 3.2a. Such a source is found in a green (532 nm), low-power Optically Pumped Semiconductor Laser (OPSL); a 100 mW Sapphire™ laser from Coherent Inc. is used in the microscope, see Table 3.1.

It was found that the output of this laser is slightly elliptical, which we corrected by the use of a single mode fibre as a spatial mode filter. Coupling the free-space output of the laser into fibre affords additional advantages. Neutral density filters can be easily placed in the free-space laser path before the fibre for attenuation of the laser power (*e.g.* for providing faint illumination during alignment and to extend the life of optical components during operation). As well, the fibre provides alignment modularity as its output end is minimally affected by changes made to the input end of the fibre (*e.g.* for alignment tweaking or installation of new optical components).

Achieving high-quality fibre coupling to single-mode fibre is challenging. The beam at the face of the fibre must have the same spatial mode diameter as the fibre core. Further, the beam wavefront must have an infinite radius of curvature at the fibre face, *i.e.* it must be focused on the fibre face, to achieve high coupling efficiency, see Figure 3.2b. Finally, the input beam must lay on the optical axis of the fibre both in translational and angular degrees of freedom, see Figure 3.2c. A single, short focal length lens; pre-packaged as a fibre-coupling component; is typically used to achieve these conditions. Fibre-couplers are available tuned to a specific wavelength. If the operational wavelength does not match the design wavelength either a custom aligned part can be ordered or pre-conditioning optics can be used with the off-the-shelf component. We chose the latter option, as the closest, off-the-shelf aligned fibre-coupler available was aligned at 543 nm, see Table 3.1.

It was found that back-of-the-envelope calculations using geometric optics were insufficient to gain insight into the design of the pre-conditioning optics. To aid in component selection and alignment a generic Gaussian beam tracing calculator was written. One approach to tracing a beam through an optical system is to use its propagating electromagnetic wave description and compute the effect of optical components on the propagating wave [57, 58]. This is difficult to do. An alternative is to use the complex-ray description of a Gaussian beam and use *ABCD* ray tracing matrices to evolve the ray [57]. A third method to directly compute the beam profile using two real rays evolved with *ABCD* matrices was developed by Jacques Arnaud and shown to be equivalent to the complex-ray description [59]. This last approach was employed in the calculator.
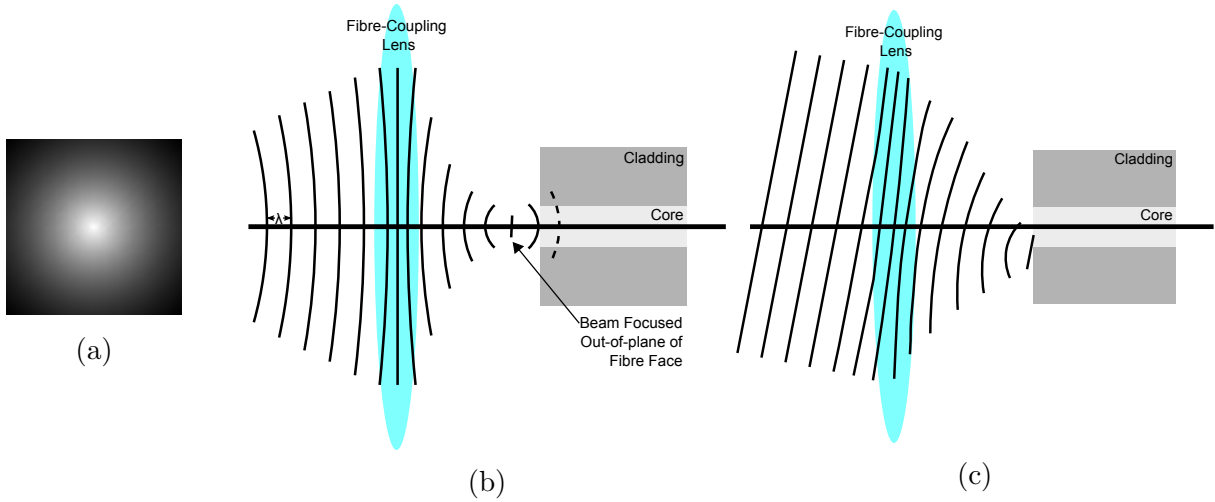
Figure 3.2: a) Illustration of a TEM_{00} spatial mode, in cross-section, drawn in *Mathematica*. b,c) Schematics of conditions for coupling a free-space beam into a single mode fibere poorly. b) The collimation of the input beam affects the wavefront shape at the face of the fibre. Poor coupling efficiency will be achieved in this configuration despite the beam's diameter matching that of the core, due to the finite wavefront curvature. c) Angle of input beam affects positioning of beam focus with respect to fibre-core as well as angle of input.

The *ABCD* ray tracing method provides a simple formalism to compute the action of optical elements on input light, represented by rays. The rays take the form:

$$\begin{pmatrix} x \\ \theta \end{pmatrix} = \begin{pmatrix} distance\ of\ ray\ from\ optical\ axis \\ slope\ of\ ray \end{pmatrix} \tag{3.1}$$

The *ABCD* matrices that act on these vectors for air and lens will be of interest for the calculator. They are, with d distance travelled through the air and f focal length, respectively [54]:

$$\mathbf{Air} = \begin{pmatrix} A & B \\ C & D \end{pmatrix} = \begin{pmatrix} 1 & d \\ 0 & 1 \end{pmatrix} \tag{3.2}$$

$$\mathbf{Lens} = \begin{pmatrix} 1 & 0 \\ -\frac{1}{f} & 1 \end{pmatrix} \tag{3.3}$$

The Arnaud method takes advantages of this simplicity. The beam intensity profile,

$w(z)$, is defined as the distance from the optical axis where the intensity of the Gaussian beam reduces to $^1/e^2$, see Figure 3.3a. The profile of the beam is hyperbolic with asymptotes inclined at an angle of $\theta = \frac{\lambda}{\pi w_0}$ [57]:

$$w^2(z) = w_0^2 \left[1 + \left(\frac{\lambda z}{\pi w_0^2} \right)^2 \right] \tag{3.4}$$

where w_0 is the beam waist, λ is the wavelength of the light, and the z-axis is the optical axis, see Figure 3.3b. This profile can be reproduced by the two rays of Arnaud, see again Figure 3.3b. The first ray begins at the beam waist position, $z = 0$, on the optical axis and is inclined at the asymptote angle, θ:

$$\xi = \begin{pmatrix} 0 \\ \frac{\lambda}{\pi w_0} \end{pmatrix} \tag{3.5}$$

Th second ray begins at the beam waist at $z = 0$ and is parallel to the optical axis:

$$\eta = \begin{pmatrix} w_0 \\ 0 \end{pmatrix} \tag{3.6}$$

Then, the profile is computed from the x-components of the two rays:

$$w = \sqrt{\xi_x^2 + \eta_x^2} \tag{3.7}$$

Consider the evolution of the beam through air:

$$\xi' = \begin{pmatrix} 1 & z \\ 0 & 1 \end{pmatrix} \begin{pmatrix} 0 \\ \frac{\lambda}{\pi w_0} \end{pmatrix} = \begin{pmatrix} \frac{z\lambda}{\pi w_0} \\ \frac{\lambda}{\pi w_0} \end{pmatrix}, \eta' = \begin{pmatrix} 1 & z \\ 0 & 1 \end{pmatrix} \begin{pmatrix} w_0 \\ 0 \end{pmatrix} = \begin{pmatrix} w_0 \\ 0 \end{pmatrix} \tag{3.8}$$

Using equation 3.7 we find the beam profile is reproduced:

$$w(z) = \sqrt{\left(\frac{z\lambda}{\pi w_0} \right)^2 + w_0^2} = \sqrt{w_0^2 \left[1 + \left(\frac{z\lambda}{\pi w_0^2} \right)^2 \right]} \tag{3.9}$$

The calculator based on this formalism was written in *Mathematica*, see Appendix A for the code. While in principal the effect of diffraction, aberrations, and non-ideal alignment can also be simulated, in practice it is a much better idea to use the output of a calculator such as this one as a very good starting point and to perform the fine-alignment in the
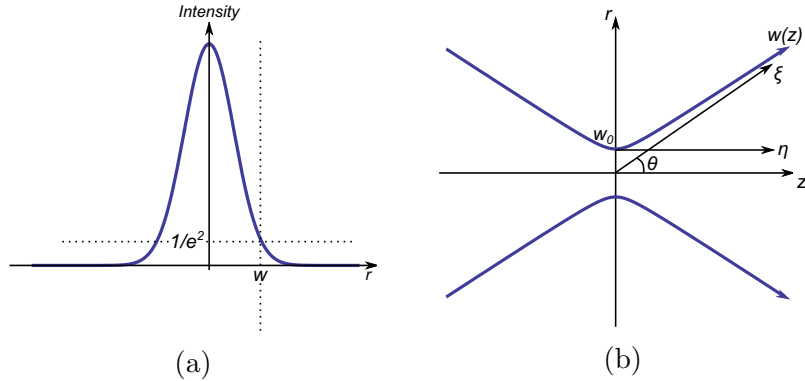
physical apparatus.

Figure 3.3: a) A Gaussian beam shown in schematic cross-section. The beam radius, $w(z)$, is illustrated. b) A Gaussian beam in profile, showing schematically the hyperbolic shape of the beam. The real rays of Arnaud are also shown, $\theta = \lambda/\pi w_0$ [59]. Here the z-axis is the optical axis and the r-axis is radial distance from the optical axis.

From the calculator, a 2x magnification preconditioning telescope consisting of 50 mm and 100 mm plano-convex lenses is selected and implemented, see Figure 3.7. Two mirrors on tip-tilt mounts are additionally used to provide convenient access to four degrees of freedom of the beam at the fibre-face: tip, tilt and translation perpendicular to the optical axis, see Figure 3.12. The coupling efficiency achieved is $\gtrsim 66\%$. This was calculated simply by measuring the optical power out of the fibre with a power meter and dividing it by the measured power before the fibre. As the fibre has a maximum insertion loss of 1.5 dB [60], or 71%, this efficiency corresponds to very good alignment.

Switch Arm

Coherent control experiments with NV centres call for the laser excitation to be turned on and off on demand with switching times on the order of tens of nanoseconds. This could be achieved with a pulsed laser at the cost of apparatus complexity. Instead, the laser is operated in continuous wave mode and its output manipulated with an Acousto-Optic Modulator (AOM) that we purchased from Isomet Corp., see Figure 3.12 and Table 3.1.

An AOM consists of an optical medium and a piezoelectric material joined together, see Figure 3.5a. When the piezoelectric device is driven with a radio-frequency signal it oscillates mechanically, subsequently causing mechanical oscillations in the optical medium. The compression and rarefaction of the material cause changes in the index of refraction of
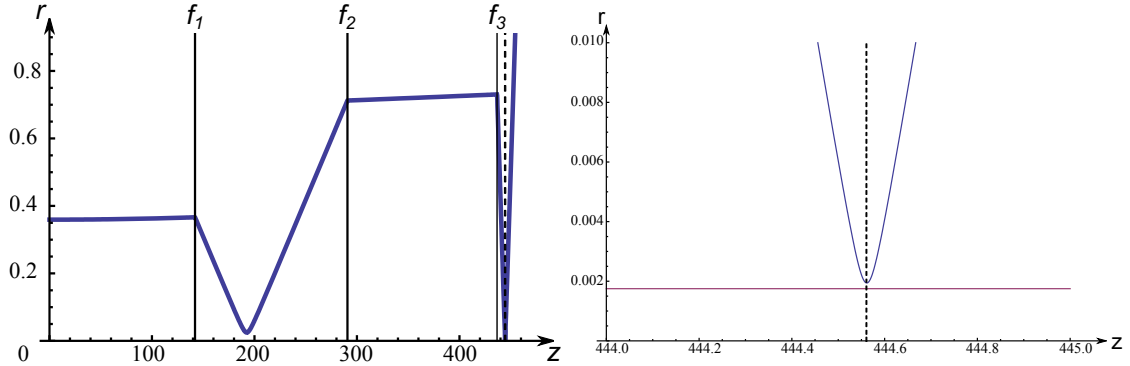
13

Figure 3.4: a) The output of the beam tracing calculator, f_i are lenses of focal length $\{50, 100, 7.85\}$ mm, respectively, the dotted line is the location of the fibre face and all distances are in millimeters. b) A close up at the fibre face, horizontal line indicates fibre core radius.

the optical medium, resulting in a transmission diffraction grating forming in the medium. Light will diffract when it is incident on this grating at the Bragg angle,

$$\theta_{Bragg} = \arcsin\left(\frac{n\lambda}{2d}\right) = \arcsin\left(\frac{n\lambda}{2}\frac{f_{rf}}{v}\right), \tag{3.10}$$

where n is the diffraction peak order, λ is the wavelength of the incident light, d is the grating period, f_{rf} is the frequency of the radio-frequency signal, and v is the velocity of the acoustic wave in the optical medium. The optical medium in our AOM is TeO_2, supporting an acoustic velocity of $v = 4.21$ mm/μs and $f_{rf} = 200$ MHz [61]. The resulting Bragg angle is $\theta_{Bragg} = 0.72°$ and the separation between the 0th and 1st orders is $2\theta_{Bragg} = 1.44°$. Thus, over a distance of 250 mm, the distance between these two orders will be ~6 mm. The angle of incidence and intensity of the grating can be tuned to cause approximately half the incident light to be scattered to the first order diffraction peak.

To use the AOM as a switch the first order diffraction peak is picked off with an iris. Thus, when the AOM is on light gets through the iris, whereas when it is off it is blocked, see Figure 3.5b. This method results in an on-off intensity ratio of ~300:1 caused by leakage through the iris, due to the spatial extent of the diffraction peaks and iris construction. A double pass AOM configuration is used to improve the on-off intensity ratio to ~24,000:1. The first order peak is still picked off with an iris and then is reflected off a mirror along the same path it travelled from the AOM. This returning path satisfies the Bragg condition of the AOM and its first order diffracted peak travels along the path followed by the original
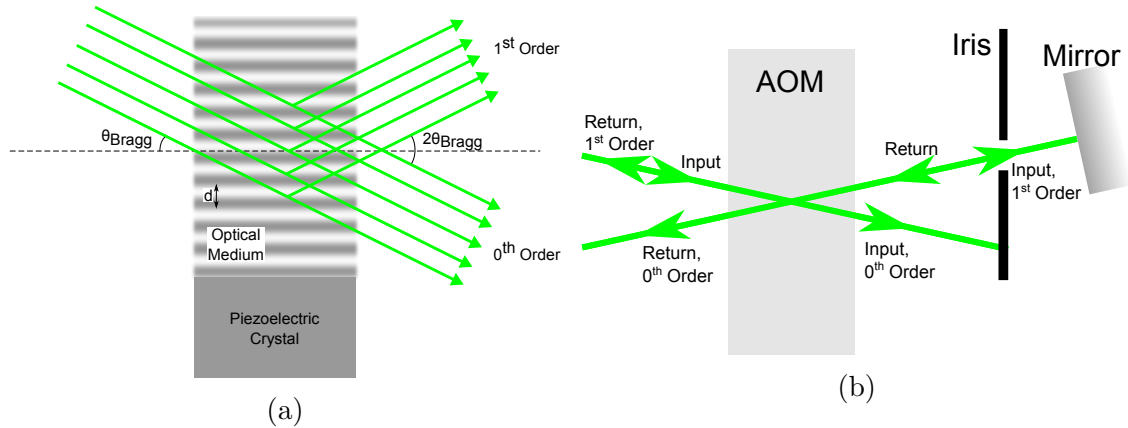
14

Figure 3.5: a) The principle of an AOM. The input optical beam scatters off the acoustic grating and constructively interferes when the Bragg condition is met (see main text). b) The AOM used as a switch.

input beam, see Figure 3.5b. A beam splitter and a second iris complete the double-pass set-up, see Figure 3.12. Scattering from the internal faces of this beam-splitter and other optical components is the main reason that the double-pass configuration achieves a on-off intensity ratio that is a little less than the square of the single-pass on-off intensity ratio.

The switching time of the AOM is limited by the time the acoustic wave takes to propagate across the beam in the optical medium. Thus, the fastest switching time is achieved for the smallest beam size. A competing constraint is the efficiency of diffraction. A larger beam interacts with more acoustic fringes, making the diffraction effect stronger. From Isomet's specifications, see Figure 3.6, a beam diameter of 80 μm results in a switching time of ~12 ns and $\gtrsim$ 80% AOM efficiency [61], which satisfy the switching requirements of the microscope. To achieve this input beam at the AOM, the AOM is placed at the focus of a telescope formed with plano-convex lenses of focal lengths 175 mm and 150 mm, see Figure 3.12. The choice of lenses was due to the output beam diameter of the fibre-coupled laser, which is ~1.6 mm and the requirement of the mode-shaping arm described below. See Figure 3.8 for the output of the beam tracing calculator used to select these components.

Finally, to improve the through-put of light in the switching arm we take advantage of the polarization of the light. Instead of a beam splitter, a polarizing beam splitter (PBS) is used. The laser output begins as linearly polarized, the polarization of which is maintained by the fiber used. A $\lambda/2$-waveplate (HWP) is used to rotate the polarization to be p-polarized with respect to the PBS, which the PBS is designed to transmit. Following the AOM a 45°-rotated $\lambda/4$-waveplate (QWP) is used to convert the p-polarized light to
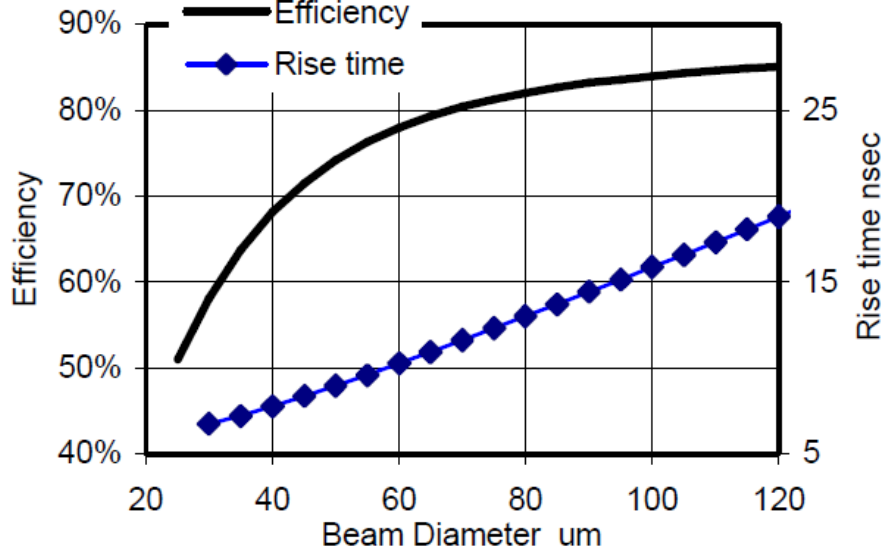
Figure 3.6: The rise time and switching eficiency of the AOM, reproduced from the AOM datasheet provided by ISOMET Corp. [61]

circularly polarized light. The mirror causes the handedness of the circularly polarized light to reverse and the QWP, which is now rotated $-45°$ from the perspective of the beam, converts this to s-polarized light with respect to the PBS, as seen with the use of the respective Jones matrices [54]. The Jones matrix for a rotated QWP is:

$$Q(\theta) = R(\theta).Q.R(-\theta) \tag{3.11}$$

$$= \begin{pmatrix} \cos(\theta) & \sin(\theta) \\ -\sin(\theta) & \cos(\theta) \end{pmatrix} \begin{pmatrix} e^{i\pi/4} & 0 \\ 0 & e^{i3\pi/4} \end{pmatrix} \begin{pmatrix} \cos(\theta) & \sin(\theta) \\ -\sin(\theta) & \cos(\theta) \end{pmatrix} \tag{3.12}$$

$$= \begin{pmatrix} \frac{i+\cos(2\theta)}{\sqrt{2}} & \sqrt{2}\cos(\theta)\sin(\theta) \\ \sqrt{2}\cos(\theta)\sin(\theta) & -\frac{-i+\cos(2\theta)}{\sqrt{2}} \end{pmatrix} \tag{3.13}$$

16

Figure 3.7: a) The output of the beam tracing calculator, f_i are lenses of focal length $\{7.85, 175, 150\}$ mm, respectively. The origin is at the output fibre face of the source, the first dotted line is the location of the AOM centre, and the second dotted line is the location of the fibre face of the mode shaping arm, and all distances are in millimeters. b) A close up at the mode shaping arm input fibre face, horizontal line indicates fibre core radius.

Figure 3.8: a) The output of the beam tracing calculator.

where $R(\theta)$ is a rotation matrix. Substituting $45°$ and $-45°$ into $Q(\theta)$ results in:

$$Q(\pi/4) = \begin{pmatrix} \frac{i}{\sqrt{2}} & \frac{1}{\sqrt{2}} \\ \frac{1}{\sqrt{2}} & \frac{i}{\sqrt{2}} \end{pmatrix} \tag{3.14}$$

$$Q(-\pi/4) = \begin{pmatrix} \frac{i}{\sqrt{2}} & -\frac{1}{\sqrt{2}} \\ -\frac{1}{\sqrt{2}} & \frac{i}{\sqrt{2}} \end{pmatrix} \tag{3.15}$$

Thus, the action of the QWP, mirror, and QWP again on a p-polarized input is to transform

17

it to s-polarized, up to a global phase:

$$Q(-\pi/4).M.Q(\pi/4).p \tag{3.16}$$

$$= \begin{pmatrix} \frac{i}{\sqrt{2}} & -\frac{1}{\sqrt{2}} \\ -\frac{1}{\sqrt{2}} & \frac{i}{\sqrt{2}} \end{pmatrix} \begin{pmatrix} 1 & 0 \\ 0 & -1 \end{pmatrix} \begin{pmatrix} \frac{i}{\sqrt{2}} & \frac{1}{\sqrt{2}} \\ \frac{1}{\sqrt{2}} & \frac{i}{\sqrt{2}} \end{pmatrix} \begin{pmatrix} 1 \\ 0 \end{pmatrix} \tag{3.17}$$

$$= -i \begin{pmatrix} 0 \\ 1 \end{pmatrix} \tag{3.18}$$

$$= -is \tag{3.19}$$

Thus, after the return path is diffracted by the AOM, it will reflect off the PBS into the second iris, see Figure 3.12.

Mode Shaping Arm

After passing through the two blocking irises of the switching arm the spatial mode of the beam has significant aberrations. A single mode fibre is used again as a mode filter. The telescope of the switching arm already provides the necessary degrees of freedom to couple into another fibre-coupler, which is the same model used with the laser, see Figure 3.8.

The filtered output of the fibre is coupled to free space with another fibre-coupler of the same model as the input. The output face of this fibre marks the first point that must be maintained conjugate to the focal plane of the microscope objective. This will ensure that the green illumination is confocal with the red collection path to be described below.

Next, the beam is expanded from its initial 1.6 mm to 4 mm with a 2.5x magnification telescope, using 50 mm and 125 mm focal length plano-convex lenses, to under-fill the 5 mm aperture of the scanning mirrors described below. This telescope together with the scanning telescope described below was carefully aligned to ensure the output beam from this telescope is well collimated to satisfy the requirements of the infinity corrected objective, see below. Figure 3.9 shows the output of the beam calculator used to achieve this effect.

The output of the mode shaping arm feeds into the scanning optics below by being reflected off of a dichroic mirror. The dichroic mirror used has a sharp reflection at the green 532 nm wavelength and allows wavelengths from 550 to 825 nm to pass, see Figure 3.11. Thus, all red emission from the NV is transmitted to the detector, see Figure 3.12.
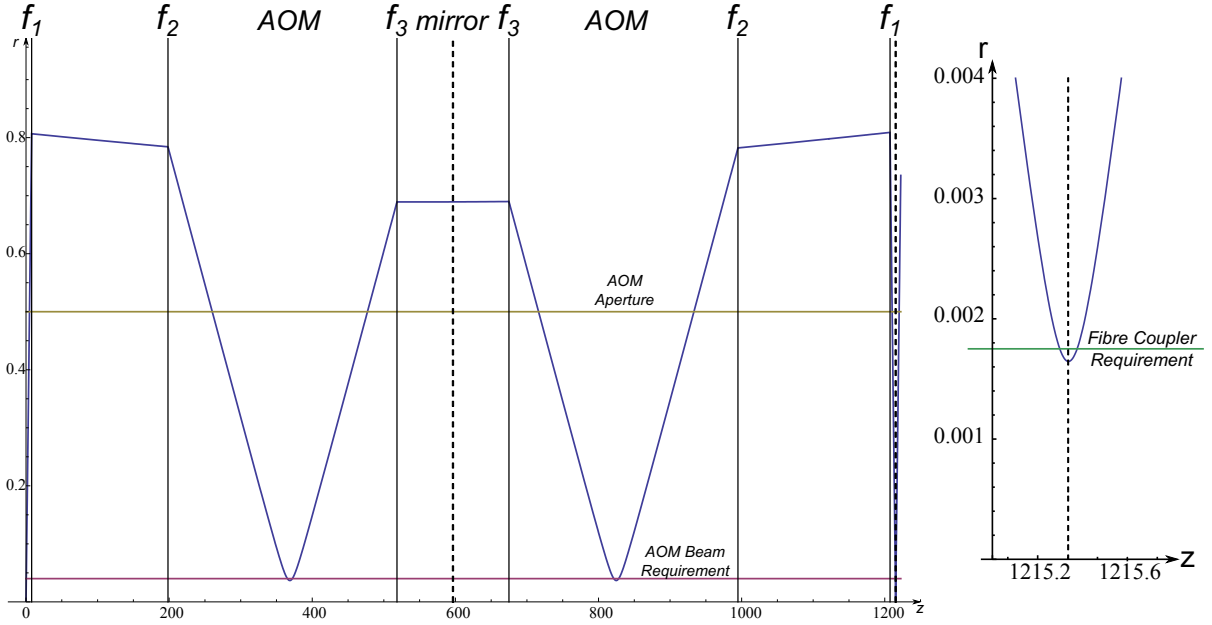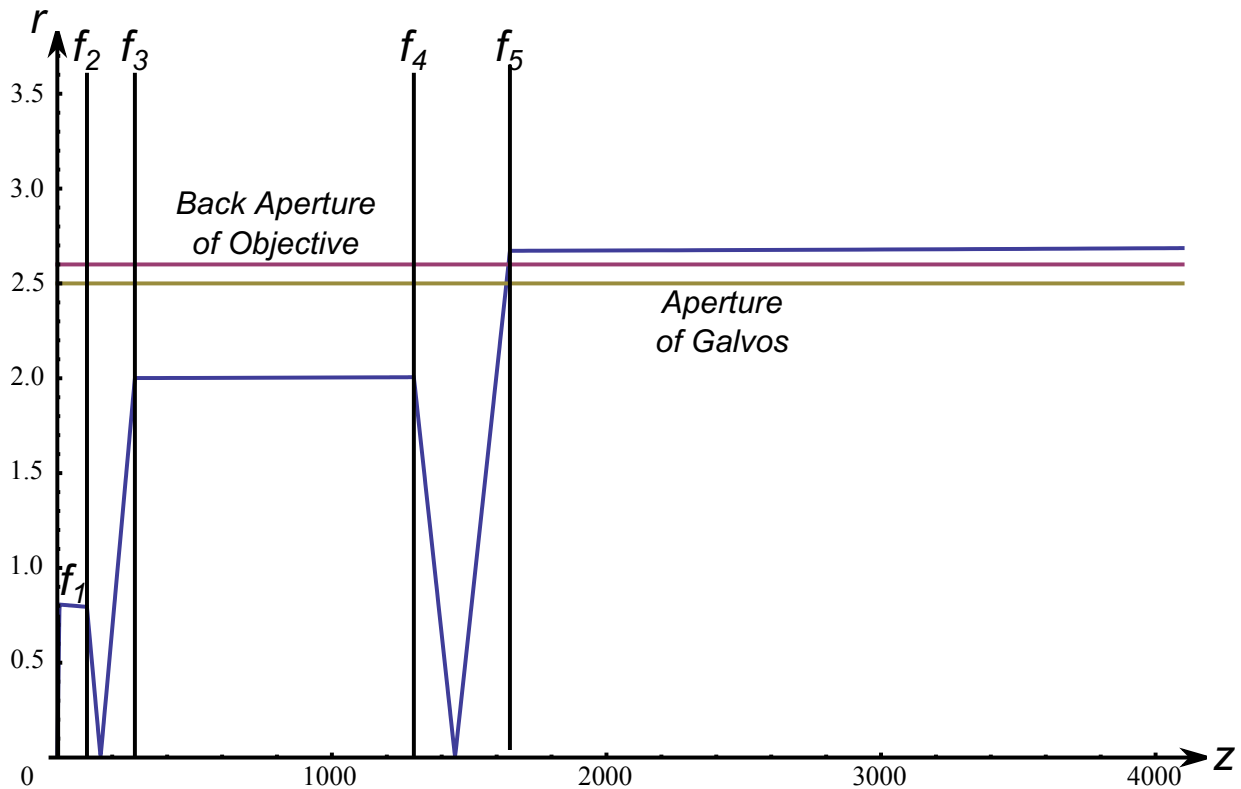
Figure 3.9: The output of the beam tracing calculator, f_i are lenses of focal length $\{7.85, 50, 125, 150, 200\}$ mm, respectively. The position of the first lens is not well resolved over the 4 m scale of this plot. The origin is at the output fibre face of the mode shaping arm. The second and third lenses constitute the telescope for the mode shaping arm. The last two lenses make the scanning telescope. Notice that the output of the scanning telescope is well collimated over a range of > 2 m. All distances are in millimeters.

Scanning Optics

The scanning optics consist of scanning mirrors mounted on galvanometers (galvos), a scanning telescope and the objective. The objective is infinity corrected, meaning it requires as input a collimated beam, which it will focus to a spot in its focal plane. If, instead of being parallel to the optical axis, the input beam enters the back of the objective at an angle then the objective will focus the beam in the focal plane, but off the optical axis, see Figure 3.10a. To achieve this with a beam source fixed in space, a scanning telescope and galvos are employed. The pivot of the galvos is placed in a conjugate plane to the back of

the objective through the scanning telescope, see Figure 3.10b.

The constraints on the alignment of the scanning telescope are as follows, distances and focal lengths are shown in 3.10b [62]:

1. To maintain the collimation of the input beam the telescope condition must be met, which states that the lens separation, d_2, is the sum of the focal lengths of the lenses:

$$d_2 = f_1 + f_2 \tag{3.20}$$

2. To make the galvo pivot conjugate with the back of the objective d_1 must be related to d_3 by:

$$d_1 = \frac{f_1^2}{f_2} + f_1 - d_3(\frac{f_1}{f_2})^2 \tag{3.21}$$

This expression is found by tracing a ray, representing the entire optical beam, emanating from the optical axis at d_1 and intersecting the optical axis again at d_3 using the $ABCD$ ray tracing matrices of equations 3.2 and 3.3. Setting $x_{galvos,objective} = 0$, substituting in equation 3.20, and solving for $d1$ in the following yields expression 3.21:

$$\begin{pmatrix} x_{objective} \\ \theta_{objective} \end{pmatrix} = \mathbf{Air}(d_3).\mathbf{Lens}(f_2).\mathbf{Air}(d_2).\mathbf{Lens}(f_1).\mathbf{Air}(d_1). \begin{pmatrix} x_{galvos} \\ \theta_{galvos} \end{pmatrix} \tag{3.22}$$

3. Under the approximations of geometric optics a lens can focus an input beam to an infinitesimal point. In reality the size of the focal spot will be limited by the wave-nature of light. For a Gaussian beam the ratio of beam waists in the conjugate planes of an optical system is given by the magnification of that system: $w_{0,in}/w_{0,out} = M$ [63]. As the input to the infinity-corrected objective will be collimated, see Figure 3.9, the smallest, diffraction limited focal spot will be achieved when the input beam fills the aperture of the objective as this limits the input beam waist. To ensure that this is the case with the objective, the input beam is made slightly larger than the back aperture of the objective, overfilling it. Overfilling gives the added benefit of giving some leeway in aligning the galvo pivot and objective to be conjugate.

On the other, the smaller the mirrors that are used on the galvos the higher the scanning speed can be made. Thus, an additional constraint on the scanning telescope

is to magnify the beam from the galvos to overfill the back of the objective:

$$M_{telescope} = \frac{D_{overfilled\ objective}}{D_{galvos}} = \frac{f_2}{f_1} \qquad (3.23)$$

In the physical apparatus a Nikon 100x magnification, oil immersion objective with a Numerical Aperture (NA) of 1.3 is used. It has a focal length of 2 mm [64] leading to a back aperture of $2 \times 2 \times 1.3 = 5.2$ mm. Galvos from Cambridge Technologies with aperture of 5 mm are used and are under-filled with a 4 mm beam (see the mode shaping arm above) to accommodate scanning. Thus, to satisfy constraint 3 a telescope with magnification 1.3x is used. Nikon recommends a distance of 100-200 mm between the telescope and objective [65] to minimize chromatic aberrations. Notice, that if d_3 is set equal to f_2, equation 3.21 reduces to $d_1 = f_1$. Thus, to satisfy constraints 2 and 3 and Nikon's recommendation the telescope is implemented with $f_1 = 150$ mm and $f_2 = 200$ mm plano-convex lenses and $d_3 = 200$ mm, see Figure 3.9 for the beam tracing calculator output. As the telescope is on both the red and green paths achromatic lenses are chosen. While all other lenses are mounted on two-axes translation stages to position the lens on the optical axis, and sometimes on a third axis for translation along the optical axis, the scanning telescope lenses are mounted on a six-axis lens-mount - three translation and three rotation. The additional degrees of freedom are necessary because during scanning the beam will be significantly off-axis, whereas the beam is located near the optical axis of all other lenses in the microscope.

The whole scanning apparatus is assembled on a raised platform to accommodate the sample stage and to conveniently have the sample mounted horizontally, see inset of Figure 3.12. This is particularly useful since the objective is an oil-immersion lens.

Sample Stage

While the galvos provide fine lateral scanning, the sample itself is translated for vertical scanning using a piezoelectric actuator. It has a range of 20 micrometers and nanometer resolution, which is more than enough to align the confocal spot with an NV.

A three-axis coarse translation stage actuated by three stepper motors provides additional flexibility. These have a range of 4 mm with sub-micrometer resolution. This allows us to work near features of interest on the sample, such as the antenna, see Figure 4.3, and deep in the diamond bulk to have highly coherent NVs. The motor actuated coarse translation also facilitates automated scanning of large portions of the diamond in search for NVs with desired properties.
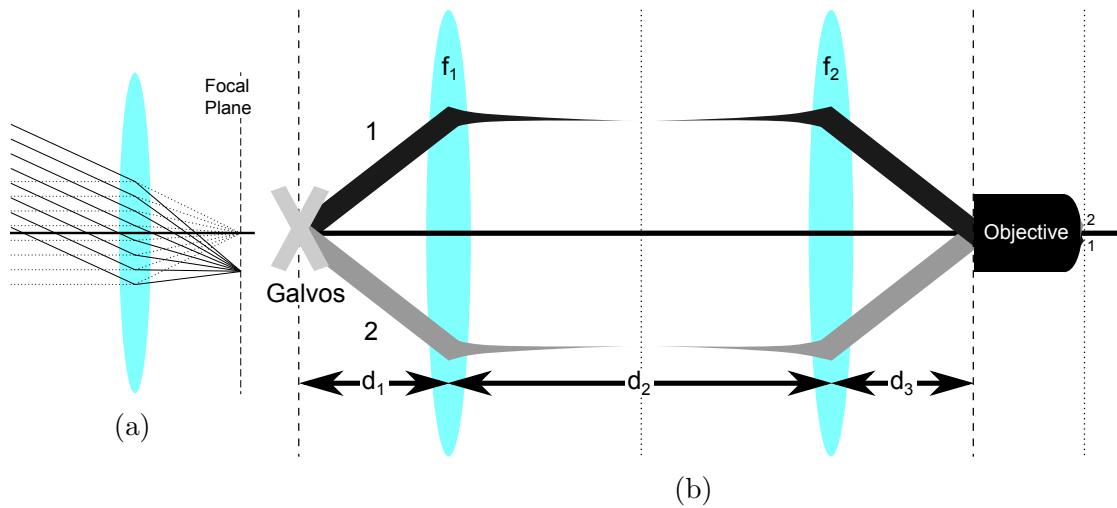
Figure 3.10: Operation of the scanning optics. a) Effect of input beam angle on focal spot position illustrated for a simple lens. b) Scanning optics set-up. Dashed lines are conjugate planes of the scanning telescope while the dotted lines are conjugate planes of the confocal system. Two beams are illustrated corresponding to two galvo configurations (the pinhole is placed on another conjugate confocal plane).

The piezoelectric actuator and three axis motors are all contained in a single unit from Thorlabs, the NanoMax300, see Table 3.1. The NanoMax stage is mounted on yet another vertical translation stage with a 20 mm range. This last stage makes initial sample mounting and coarse alignment convenient.

Pinhole Detector

Light returning from the sample, be it emitted or reflected light, travels back along the scanning telescope and to the dichroic mirror where wavelengths between 550 and 825 nm are transmitted to the pinhole ('red' for convenience). Two more filters, a sharp notch filter and a broader notch filter, centred at 532 nm are used to further block green laser reflections from entering the detector, see Figure 3.11.

The core of a single-mode (SM) fibre acts as the pinhole in this microscope. A fibre-coupling lens is used to focus the red input onto the core of the fibre. The focal plane of this lens and that of the objective are conjugate planes. Due to the strict constraints on the acceptable input to the SM fibre, see Figure 3.2, the fibre core does not admit off-axis and out-of-plane plane point sources from the sample, producing the confocal condition.
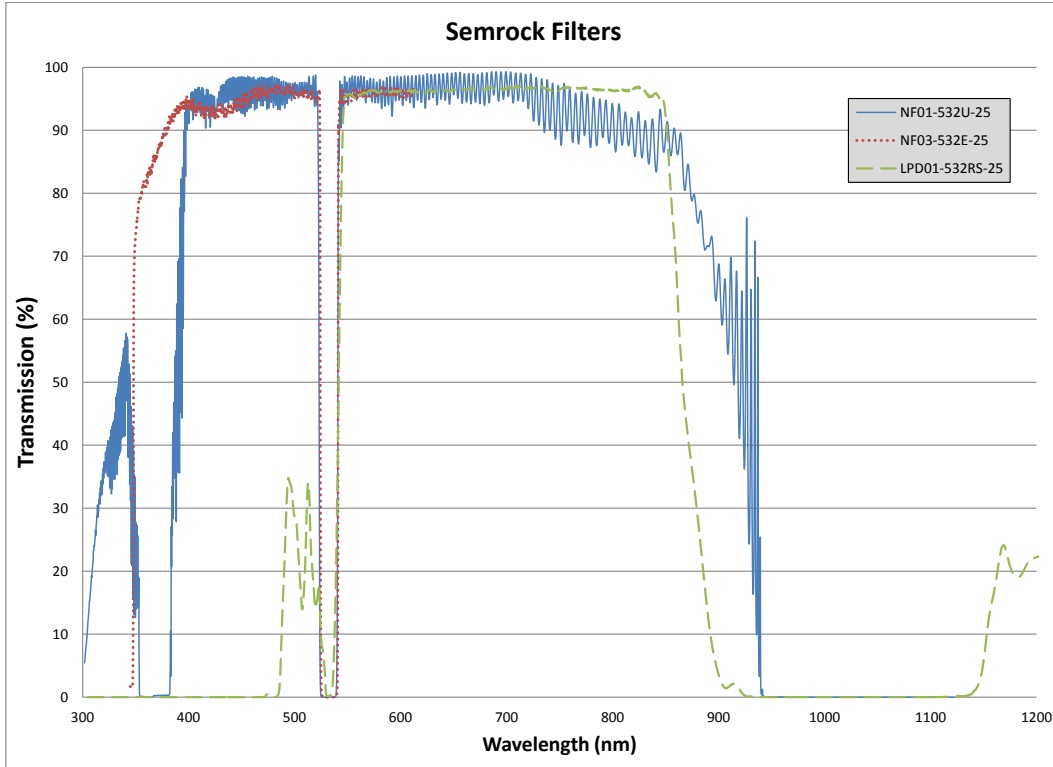
Figure 3.11: The performance of the dichroic (LPD01) and the two additonal filters as found on the Semrock, Inc. website [66]

The alignment of this fibre is checked by coupling a red diode laser in the reverse direction and aligning the red and green paths in the scanning apparatus to be concentric and co-collimated over distances of on order 10 m. Thus, the green illumination and the red collection will be confocal as well.

Since the NV is a single atomic defect and diamond has a high index of refraction the output from a single NV is faint - typically less than a photon per experiment on average. Thus, a Single Photon Counting Module is used as the detector, consisting of an avalanche photo diode and bought from Excelitas, see Table 3.1. Each experiment is performed millions of times leading to counts per second of 10 kcps, so the dark counts rate chosen

23

for the detector is 250 cps.

Software

Software control of the various components is achieved with home-built software primarily written by Jonathan Hodges for another confocal microscope built in the group previously. The software was modified and ported to work with the current microscope primarily by Ian Hincks.

Component	Manufacturer	Part Number	Diagram
Laser	Coherent Inc.	Sapphire 532-100 CW	a
Kinematic Mount	Thorlabs Inc	Polaris-K1	b
Mirrors	Thorlabs Inc	BB1-E02	c
Neutral Density Filters	Thorlabs Inc	NE60A NE20A NE13A NE10A NE05A NE03A NE06A, permanent	d
Filter Wheel	Thorlabs Inc	FW1A	d
Iris	Thorlabs Inc	ID25 for switch arm, interchangeably ID25 and ID12 for rest	e
Lenses	Thorlabs Inc	f_1: LA1131-A f_2: LA1509-A f_3: LA1229-A f_4: LA1433-A $f_5 = f_1$ f_6: LA186-A f_7: AC254-150-B f_8: AC254-200-B f_9: AC060-010-B-ML	f_i
Lens Mount	Newport Corp.	LA1V-XY	g
Translation Stage	Newport Corp.	UMR25, stage BM11.25, micrometer M-PBN5, base plate	h

Fibre Coupler	Thorlabs Inc	F240FC-A 543 nm	i
Polarization Maintaining Single Mode Fibre	Thorlabs Inc	P1-488PM-FC-2	j
Rotating Mount	Thorlabs Inc	RSP1	k
Half Wave Plate	Thorlabs Inc	WPMH05M-532	m
Quarter Wave Plate	Thorlabs Inc	WPMQ05M-532	n
Polarising Beam Splitter	Newport Corp.	05BC16PC.3, PBS 9411, mount	o
Beam Block	Thorlabs Inc	LB1	p
Acousto Optic Modulator	Isomet Corp. Newport Corp.	1250C-848, AOM 9071, mount	q
Dichroic Mirror	Semrock, Inc. Thorlabs Inc	LPD01-532RS-25, dichroic KM100T, mount	r
Pellicle Beam Splitter	Thorlabs Inc	BP145B1, BS BP107, mount FM90, flip mount	s
Galvos	Cambridge Technology	6210HM40, scanner 6010-29-120, cables 67321H-1, driver 6102105R20, mirror mount 6M2005S20F025S1, mirrors	t
6DoF Lens Mount	Thorlabs Inc	K6X	u
Objective	Nikon	Plan Fluor 100x 1.3 NA oil immersion	v
Sample Holder	In-house	-	x
Motor and Piezoelectric Stage	Thorlabs Inc	MAX341, stage BSC103, motor controller TPZ001, piezo driver TSG001, strain gauge reader CA2906, piezo cable TPS002, piezo power supply	y

		MVN80, stage	
Manual Stage	Newport Corp.	BM17.25, micrometer	z
		M-PBN8, base plate	
		MB1236, breadboard	
Raised Optical Breadboard	Thorlabs Inc	P10, P1, thick posts	aa
		PB1, post bases	
Diagnostic Camera	Thorlabs Inc	DCC1645C	ab
Filters	Semrock, Inc.	NF03-532E-25, Sharp Notch	ac
		NF01-532U-25, Broad Notch	
Red Fibre Coupler	Newport Corp.	F-91-C1, coupler	ad
		FPH-CA4, fibre chuck	
Long Lens Mount	Thorlabs Inc	E09RMS	ae
Single Mode Fibre	Thorlabs Inc	P1-630A-FC-2	af
Single Photon Counting Module	Excelitas Technologies Corp.	SPCM-AQRH-13-FC CDX	ag
Optical Table	Technical Manufacturing Corporation	784-436-02R, table 12-41H-84, legs	ah
Enclosures	Thorlabs Inc	XE25L12, frame RM1G, corners TB4, board SH25LP38, low-profile screws	ai
Magnet and Magnet Stage	Indigo Instruments Newport Corp.	44202-2.5, magnet MFACC, stages ESP301, conroller	aj
Sample	Element Six Ltd	Diamond is mounted on Si and then PCB with microwave striplines, see Figure 4.1	ak
USAF 1951 Resolution Test Standard	Edmund Optics Inc.	38257	-

Table 3.1: Components of confocal microscope, refer to Figure 3.12.

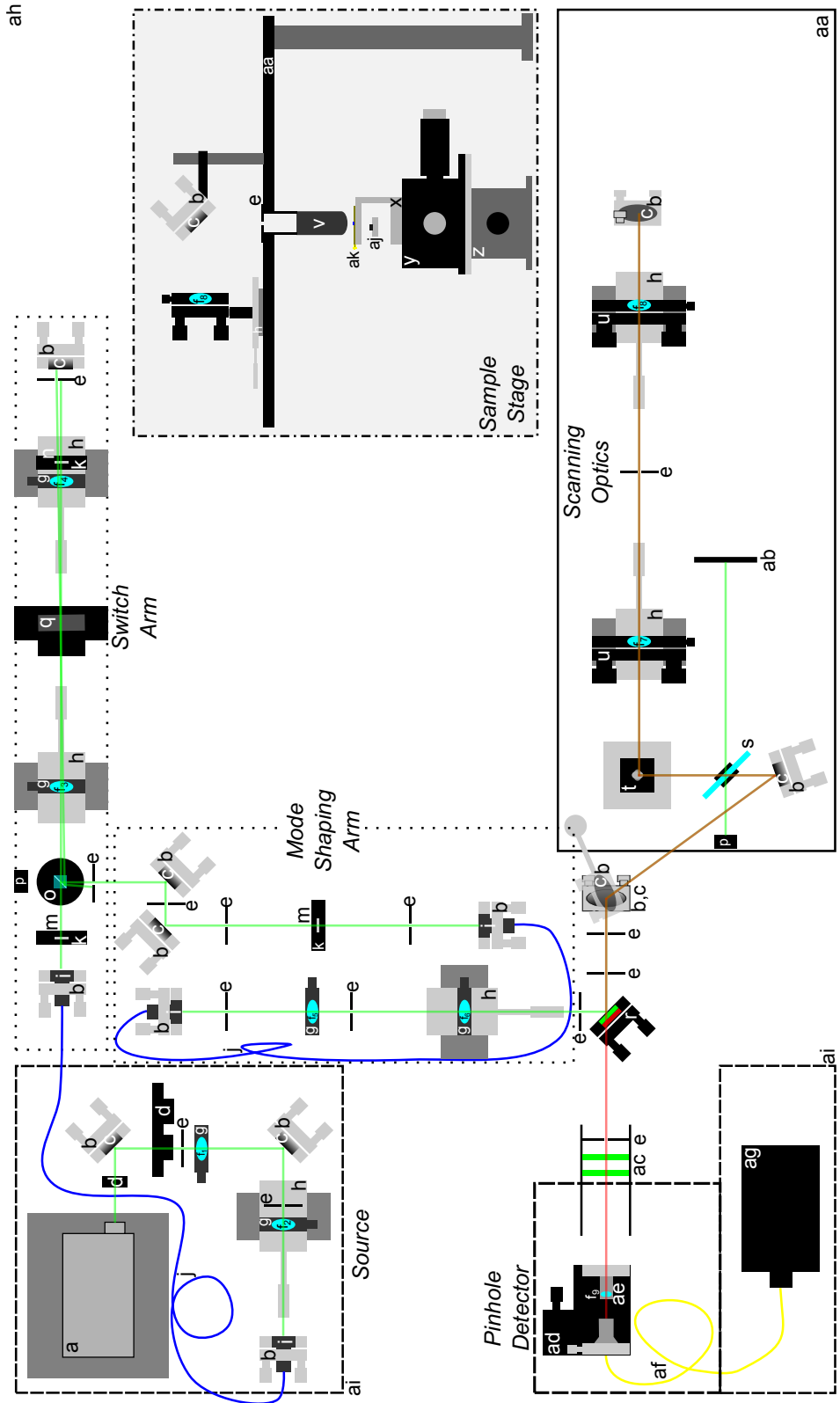Figure 3.12: Confocal microscope layout. The dotted lines for the switching and mode shaping arms are guides to the eye. The dashed lines around the laser, red-fibre coupler, and detector indicate enclosures. The solid line of the scanning telescope indicates the outline of the raised optical breadboard. Inset (dash-dot outline): Side view of objective section of microscope. Labels are listed in Table 3.1.

27

3.3   Microscope in Operation

The very first images taken with this microscope were of a chrome on glass USAF 1951 resolution test standard, see Figure 3.13a and Table 3.1 [67]. The glass is seen to be fluorescing more than the chrome number. The sample was moved around using the coarse motors till a full number appeared in the chosen ~50 μm field of view. The motors were stepped in 10 μm increments and the motion of the number on screen was used to estimate the image scale. We identified this as element 3 of group 5 in the standard [67]. Figure 3.13b is a confocal scan of a typical 25 μm copper wire used as the microwave antenna in the magnetic resonance experiments described in the following chapter. The confocal nature of this microscope is apparent in that only the top of the wire is in focus.

(a)   (b)
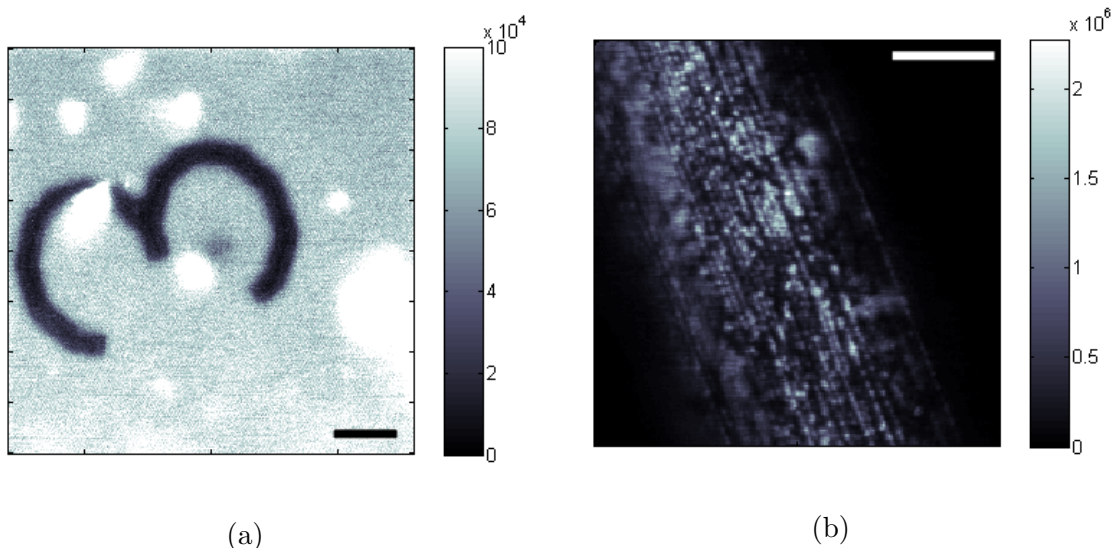
Figure 3.13: Sample images taken with the confocal microscope, scale bar is ~6 μm: a) USAF 1951 resolution test standard and b) the copper wire used to apply microwaves to the NVs. Gray scale is normalized counts per second.

We eagerly moved on to looking for NVs in diamond. Figure 3.14a is a scan containing many NVs, as confirmed by Optically Detected Magnetic Resonance studies, see next chapter. Figure 3.14b is a detailed scan of a single NV giving a nice depiction of the lateral shape of the confocal spot. We find that the lateral resolution of the microscope is $\lesssim 1$ μm, or one order of magnitude larger than the diffraction limited performance of $\sim\lambda/2 = 532/2 = 266$ nm [68]. Since extremely pure diamond samples are used it is

expected that each observed defect is in fact a single NV [52]. The spacing between NVs is observed to be of order micrometers. Thus, the resolution achieved is suitable for our experimental purposes.
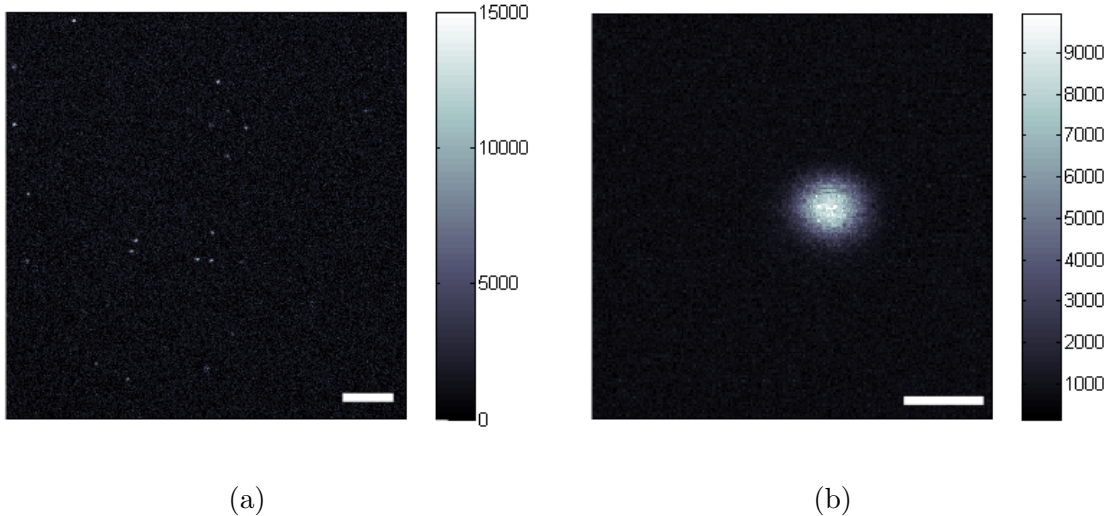

(a)   (b)

Figure 3.14: Some NVs observed with the confocal microscope a) a field of many NVs, scale bar ~6 μm b) a detailed scan of a single NV, scale bar ~1 μm. Gray scale is counts per second.

Great effort was expended to focus the laser beam to 80 μm at the AOM in order to achieve optical switching times in the tens of nanoseconds. A single NV can be used to test the timing characteristics of the microscope. We signal the AOM to turn on and gate the detector a variable delay time later to turn on for a short time, see inset of Figure 3.15a. The same figure indicates that there is a delay of ~1 μs for the AOM to turn on. The delay results from the time the acoustic wave takes to propagate to the position of the beam in the optical medium. For most conceivable NV experiments this delay can be taken into account by clever arrangement of the pulse timings. In the event that this time needs to be shortened the beam can be made to enter the optical medium closer to where the medium joins the piezoelectric crystal, giving times as short as a few hundred nanoseconds [69].

A higher resolution timing diagram is measured by reducing the gate window to 10 ns and stepping the delay in 2 ns increments, which is the limit of the control hardware (see Chapter 4), see Figure 3.15b. A rise time of ~60 ns is found, or five times the target. The path length of the optical beam, red and green paths combined starting at the AOM, is approximately 6 m, leading to a delay of ~20 ns. In addition the excited state lifetime of

29

the NV is ~13 ns [39]. Finally, the 10 ns detector window is convoluted with the true rise time of the AOM. From Figure 3.15b I claim that the AOM rise time is $\lesssim 30$ ns, which is sufficient for the experiments reported below.
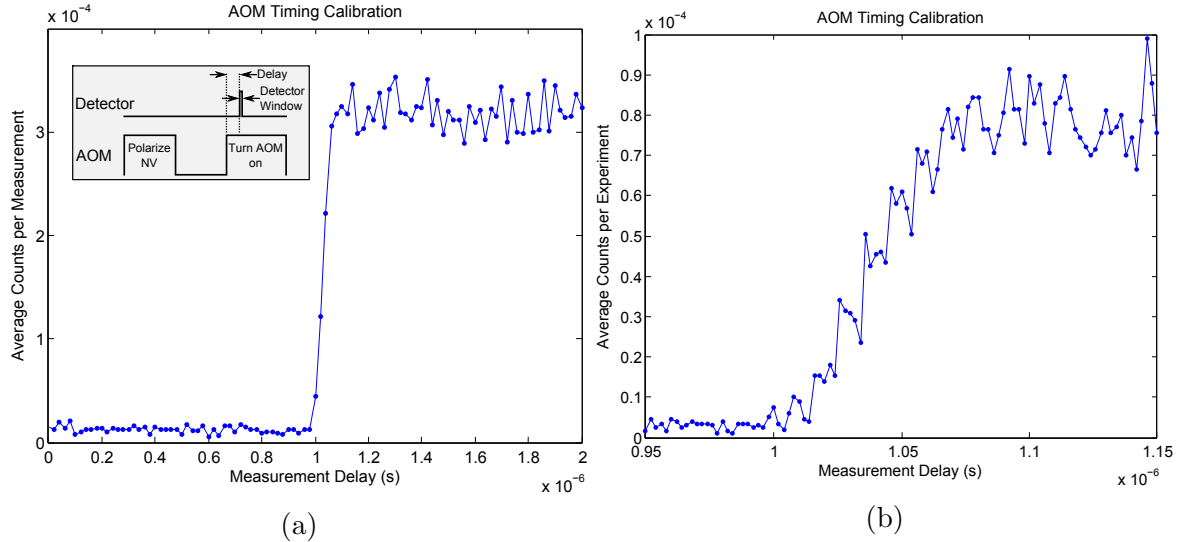

Figure 3.15: The timing characteristics of the confocal microscope. a) Gate time of 35 ns, sweeping delay in 10 ns increments, 10^6 averages. Inset: Timing diagram for experiment. b) Gate time of 10 ns, 2 ns delay increments, 2×10^6 averages.

3.4 Future Work

While this microscope performs its confocal task well, it suffers from low collection efficiency. For the $m_s = 0$ state, the NV emits a photon approximately every 13 ns, see Chapter 2. Figure 3.15a shows that over 35 ns only about 3×10^{-4} photons, on average, are collected. Thus, the collection efficiency can be estimated as ~10^{-4} per shot. The use of the single-mode fibre is a major cause of this low collection efficiency, see Figure 3.2. An alternative strategy is to use, instead of the fibre, a traditional pinhole and place it at the focus of a telescope. The detector would read the collimated, filtered output of this telescope. The less stringent mode criteria of the pinhole should dramatically improve throughput, while the confocal character of the microscope will reduce. This will be acceptable if high-purity diamond samples continue to be used as the NV-NV separation is large.

Chapter 4

Optically Detected Magnetic Resonance

In this chapter I will prove my thesis: that the instrument I have constructed can coherently manipulate single quantum systems, namely Nitrogen-Vacancy centres. The optical apparatus described in the previous chapter is used to address single NVs. That they are NVs is confirmed by measuring the characteristic magnetic resonance of NVs using the technique of Optically Detected Magnetic Resonance [52]. Pulsed microwave control of the NVs is next demonstrated, driving Rabi oscillations in the NV's ground state triplet [12]. Finally, an NV with two nearby ^{13}C nuclear spins is observed via the Ramsey spectrum of the NV [16].

4.1 Microwave Circuit

In addition to the optical handle provided by the confocal microscope precise microwave radiation must be applied to the NVs. The microwaves are delivered to the diamond sample by a 25 μm wire strapped across it. The wire is soldered to a Printed Circuit Board (PCB) with microwave launchers, see Figure 4.1. The input to the PCB is a microwave signal synthesized by a microwave frequency synthesizer. This is mixed with arbitrary digital waveforms (with a maximum frequency of 500 MHz) supplied by an Arbitrary Waveform Generator (AWG) and mixed on an IQ-mixer. As there can be noise transmitted even when the synthesizer and AWG are not supposed to produce an output, a blanking switch is used after the IQ mixer. Finally, the output signal is amplified up to 16 W and sent to

the PCB over a 2 m microwave cable to accommodate physical placement of the electronics. The microwave circuit is shown in Figure 4.1 with the parts identified in Table 4.1.

The IQ-mixer (In-phase and Quadrature-phase mixer) internal circuit is shown in Figure 4.2. The frequency synthesizer signal, the Local Oscillator (LO), is split. One branch is multiplied by the arbitrary waveform from the AWG on the I-channel, this is the In-phase arm. The other branch is phase shifted 90° and multiplied with the Q-channel. The two branches are summed and output on the 'Radio-Frequency' (RF) channel. The resulting output is:

$$I \times \cos(\omega t) + Q \times \sin(\omega t) \tag{4.1}$$

For clarity of explanation, consider the particular case when the I- and Q-channels are time-independent and of the form $I = A\cos(\phi)$ and $Q = A\sin(\phi)$. Then, the resulting signal is:

$$A\cos(\phi)\cos(\omega t) + A\sin(\phi)\sin(\omega t) \tag{4.2}$$
$$= A\cos(\omega t - \phi) \tag{4.3}$$

In this simple case the microwave circuit gives control of the amplitude, frequency, and phase of the output signal. In the general case this still applies and further the microwave synthesizer output can be shaped arbitrarily within the limitations of the AWG. In particular, this circuit allows the flexibility to apply long, low-power microwave pulses, as is required for CW-ODMR, as well as short, high-power pulses of specified phase as is required for coherent control.
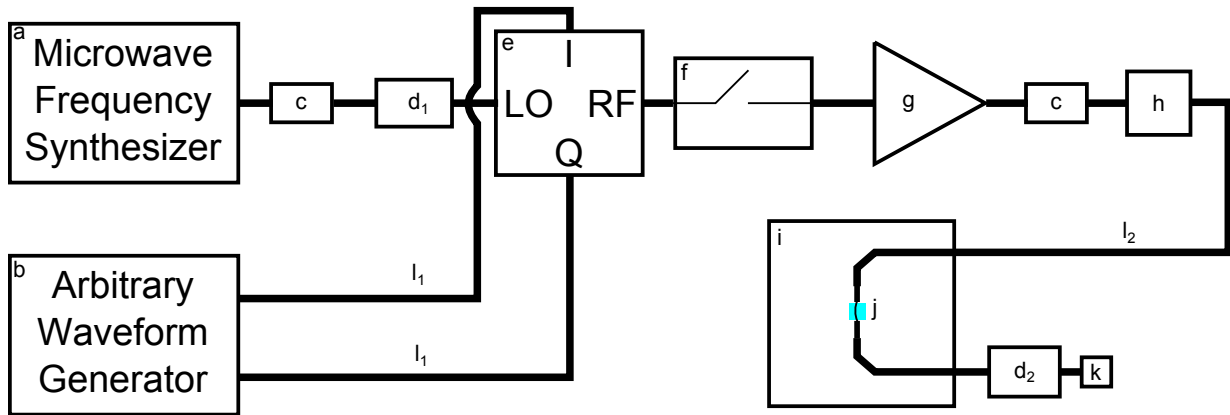
Figure 4.1: Microwave circuit layout with parts specified in Table 4.1.

Component	Manufacturer	Part Number	Diagram
Microwave Frequency Synthesizer	Phase Matrix, Inc.	FSW-0010	a
Arbitrary Waveform Generator	Tektronix, Inc	AWG5002	b
DC Block	Mini-Circuits	BLK-18-S+	c
Attenuators	Miin-Circuits	1) VAT-2W2+ 2) BW-530w20+	$d_{1,2}$
IQ Mixer	Marki Microwave, Inc.	IQ0255LMP	e
Microwave Switch	Mini-Circuits	ZYSW-2-50DR	f
Power Amplifier	Mini-Circuits	ZHL-16W-43-S+	g
Circulator	Ditom Microwave Inc.	D3C2040	h
Printed Circuit Board	-	-	i
Copper Wire Antenna	-	-	j
50 Ω Load	Advanced Technical Materials Inc.	T0516	k
Cables	-	1) Same length cables 2) ~2 m long	$l_{1,2}$

Table 4.1: Components of microwave circuit with labels corresponding to Figure 4.1.

Figure 4.2: The internal circuit of an IQ mixer.

4.2   Continuous Wave ODMR
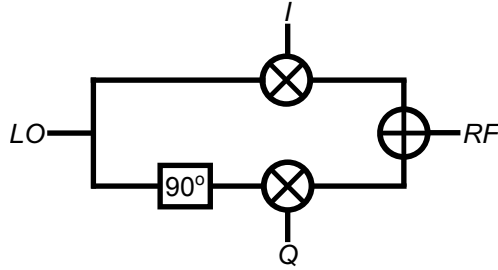
To probe the electronic structure of the NVs the synthesizer is used to apply microwaves of different frequencies to the diamond sample, see Figure 4.3. When the microwave frequency matches a difference in energy levels the microwaves are preferentially absorbed, rotating the spin state of the NVs between the corresponding levels, see Figure 4.4a. The range of frequencies used is centred about the Zero-Field Splitting, $\Delta = 2.87$ GHz, thus the $m_s = 0$ to $m_s = \pm 1$ transitions are probed, see Figure 2.1b. Instead of detecting the absorption of the microwaves directly, as is done in standard Continuous Wave Electron Spin Resonance (CW-ESR), the differential fluorescence signal from the $m_s = 0$ and $m_s = \pm 1$ levels is detected, see Figure 2.1c.

A technical issue in all NV experiments discussed here is thermal drift. As the microscope has components made of aluminium, steel, glass, *etc.* different amounts of thermal expansion and contraction cause the microscope objective to move with respect to the diamond sample as the temperature of the lab fluctuates. The result of drift is that an NV originally positioned at the confocal spot of the microscope does not remain there causing the fluorescence counts to decrease. To differentiate the effect of drift from that of applying microwaves to the NV each experiment is accompanied by a bright reference. The NV is optically pumped to its $m_s = 0$ state by shining green light on it for a time greater than the lifetime of the metastable singlet state, ~300 ns. The fluorescence is then detected, see Figure 4.4a. CW-ODMR measurements are unique in that low power microwave input is typically used to reduce the power-broadening effects and the resulting fluorescence is detected for the duration of the microwave application, typically 30 ms. For ease of comparison then, the bright reference is taken for the same length of time, far exceeding the metastable singlet lifetime of. A typical CW-ODMR spectrum of a single NV is shown in Figure 4.4b and 4.4c.
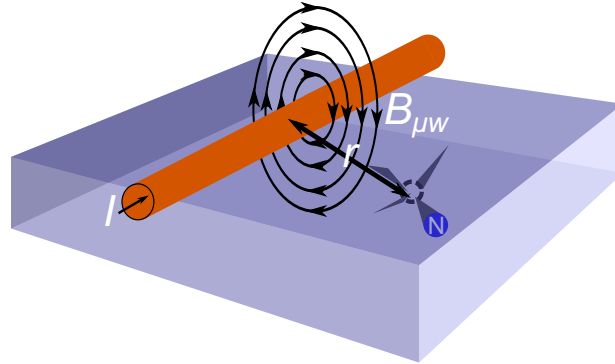
Figure 4.3: a) Microwave antenna, a 25 μm copper wire, across diamond sample. The magnitude of the oscillating microwave field at the NV is given by $B_{\mu w} = \frac{\mu I}{2\pi r}$. The orientation of the microwave vector with respect to the NV geometry is also indicated.
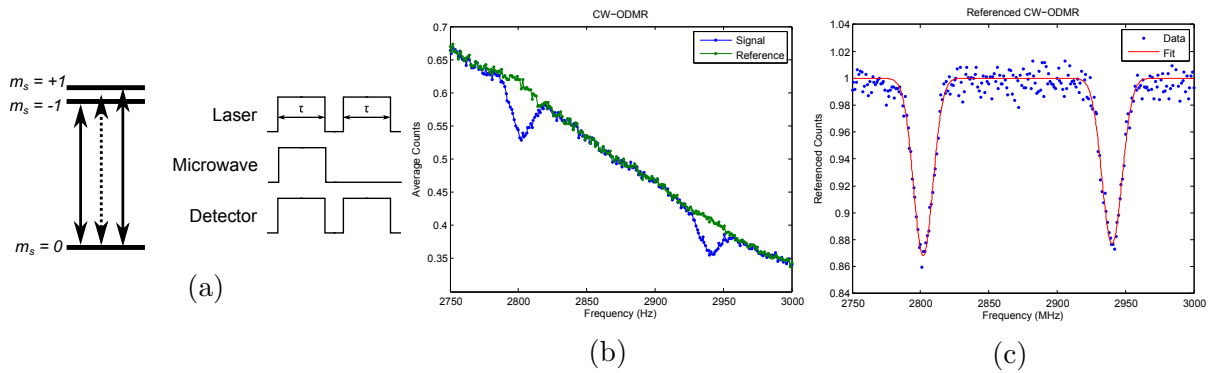
Figure 4.4: a) The first pannel illustrates the principle of magnetic resonance in the ground state triplet of the NV: when the separation in energy matches the energy of the radiation the radiation is absorbed preferentially, indicated by solid arrows. The second pannel shows the pulse sequence used for CW-ODMR, τ is typically 30 ms. b) The reference and the raw signal. c) Referenced signal. Two Gaussians were fit to the data yielding a Zeeman splitting of 138 MHz, which corresponds to a magnetic field of $\approx$ 25 G.

4.3 Pulsed ODMR

Rabi Flops Experiment

Having established that the fluorescent defects detected by the confocal microscope are indeed NVs from their CW spectra, the next task is to prove that the NVs can be coherently

manipulated. The classic experiment to prove coherent control of a quantum system is the Rabi Flop experiment. In the case of an NV, strong microwave pulses of varying duration are applied, resonant with one of the $m_s = 0$ to $m_s = \pm 1$ transitions, where the ± 1 degeneracy is lifted with an external field. We are insensitive to which transition as the Nitrogen-Vacancy axis can be parallel or anti-parallel to the magnetic field projection on the NV axis, and we arbitrarily choose $0 \rightarrow +1$ for discussion. The spin state is first optically polarized to the $m_s = 0$ level, $|\psi_{NV}\rangle = |0\rangle$. The pulses then rotate the NV spin state from a population in the $m_s = 0$ level to a superposition:

$$|\psi_{NV}\rangle = \alpha|0\rangle + \beta|1\rangle \tag{4.4}$$

where $\alpha^2 + \beta^2 = 1$ and α, β are functions of the duration of the Rabi pulse. The fluoresce signal provides a measurement in the $\{|0\rangle, |1\rangle\}$ basis. Thus, oscillations in the fluorescence signal as a function of Rabi pulse duration indicate Rabi Flops. This is indeed what is observed, as shown in Figure 4.5, for single NVs with Rabi frequencies of ~4 MHz and 13 MHz.

To understand the beating in the signal let's turn to the Hamiltonian. The Hamiltonian for the control field is time dependant:

$$H_c = \Omega \cos(\omega t + \phi) S_x \tag{4.5}$$

where S_x is as defined in equation 2.2, Ω is the amplitude of the Rabi drive, ω is the microwave frequency, and ϕ is the microwave phase and we are working in frequency units. To return to a time-independent Hamiltonian we follow the standard procedure of entering the rotating frame of the NV Larmor precession and making the Rotating Wave Approximation (RWA) [70]. Slight variations from the textbook result are seen due to the NV being quantized along S_z^2 as opposed to the familiar spin-$^1/_2$ Pauli σ_z. This result was previously worked out by Colm Ryan [71].

The full Hamiltonian, neglecting ^{13}C nuclear spins for simplicity, is:

$$H = H_{NV,N} + H_c = \Delta S_z^2 + \gamma B_z S_z + A_{N,\|} S_z \otimes I_z \tag{4.6a}$$
$$+ \Omega \cos(\omega t + \phi) S_x + \gamma \left(B_x S_x + B_y S_y \right) + A_{N,\perp} \left(S_x \otimes I_x + S_y \otimes Iy \right) \tag{4.6b}$$

Entering the rotating frame defined by the $U = e^{iH_{rot}t}$, where $H_{rot} = DS_z^2$, gives the effective interaction frame Hamiltonian:
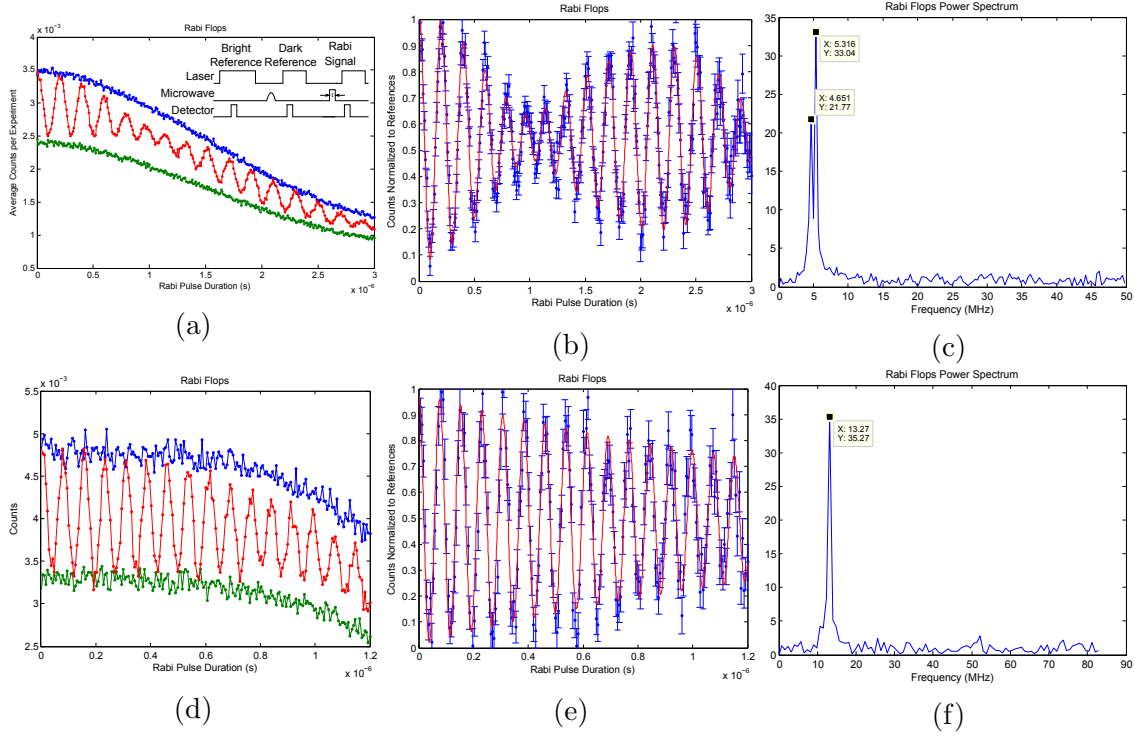
$$H_{eff} = UHU^\dagger - H_{rot} \tag{4.7}$$

Figure 4.5: a-c) An NV centre that is driven with a ~4 MHz Rabi drive. Beating due to hyperfine interaction with the ^{14}N nuclear spin is seen, see text. The data is averaged over 3.3 million experiments. d-e) An NV centre driven with a ~13 MHz Rabi drive. The data is averaged from 0.7 million experiments. a,d) Raw data showing the bright reference, signal, and dark reference. b,e) Referenced data, $^{\text{SIGNAL}-\text{DARK}}/_{\text{BRIGHT}-\text{DARK}}$, with error bars corresponding to the scaled signal divided by $\sqrt{N}$, where N is the number of experiments averaged. The fits are as described in the text. c,f) Fourier transforms of the referenced data. Inset of a) shows the pulse sequence for the Rabi experiment, the time τ is swept to obtain the Rabi signal.

The terms in equation 4.6a commute with U, while those in equation 4.6b require more analysis. We can rewrite the control Hamiltonian as [72]:

$$H_c = \Omega \frac{\sqrt{2}}{2} \left[e^{i(\omega t + \phi)S_z^2} \cdot S_x \cdot e^{-i(\omega t + \phi)S_z^2} + e^{-i(\omega t + \phi)S_z^2} \cdot S_x \cdot e^{i(\omega t + \phi)S_z^2} \right] \tag{4.8}$$

Choosing $\omega = D$, we find:

$$H_{eff} = (\Delta - D)S_z^2 + \gamma B_z S_z + A_{N,\parallel} S_z \otimes I_z \tag{4.9a}$$

$$+ \Omega \frac{\sqrt{2}}{2} \left[e^{i(2Dt+\phi)S_z^2} \cdot S_x \cdot e^{-i(2Dt+\phi)S_z^2} + e^{-i(\phi)S_z^2} \cdot S_x \cdot e^{i(\phi)S_z^2} \right] \tag{4.9b}$$

$$+ e^{iDS_z^2 t} \cdot \left(\gamma \left(B_x S_x + B_y S_y \right) + A_{N,\perp} \left(S_x \otimes I_x + S_y \otimes Iy \right) \right) \cdot e^{-iDS_z^2 t} \tag{4.9c}$$

Now we make the Rotating Wave Approximation and drop time-dependent terms leading to:

$$H_{eff} \approx (\Delta - D)S_z^2 + \gamma B_z S_z + A_{N,\parallel} S_z \otimes I_z \tag{4.10a}$$

$$+ \Omega \left[\cos(\phi)S_x + \sin(\phi)\tilde{S}_y \right] \tag{4.10b}$$

where we have also expanded the phase exponential, absorbed the $\sqrt{2}/2$ into Ω, and used the modified S_y operator:

$$\tilde{S}_y = \begin{pmatrix} 0 & -i & 0 \\ i & 0 & i \\ 0 & -i & 0 \end{pmatrix} \tag{4.11}$$

The variation from the standard spin-$^1/_2$ case is that we need to define a modified S_y operator to nicely separate the effect of the microwave phase along x and y spin axes.

Writing equation 4.10a in matrix form for the three ^{14}N spin projections and taking $D = \omega = \Delta - \gamma B_z - \delta$, i.e. the microwave is nearly resonant with the ZFS and the $m_s = -1$ NV spin projection, we have:

$$H_{m_s, N=-1} = \begin{pmatrix} 2\gamma B_z + \delta - A_{N,\parallel} & 0 & 0 \\ 0 & 0 & 0 \\ 0 & 0 & \delta + A_{N,\parallel} \end{pmatrix} \tag{4.12a}$$

$$H_{m_s, N=0} = \begin{pmatrix} 2\gamma B_z + \delta & 0 & 0 \\ 0 & 0 & 0 \\ 0 & 0 & \delta \end{pmatrix} \tag{4.12b}$$

$$H_{m_s, N=1} = \begin{pmatrix} 2\gamma B_z + \delta + A_{N,\parallel} & 0 & 0 \\ 0 & 0 & 0 \\ 0 & 0 & \delta - A_{N,\parallel} \end{pmatrix} \tag{4.12c}$$

In the limit that $2\gamma B_z \gg \delta \pm A_{N,\parallel}$ the contribution of the NV $m_s = +1$ projection will be negligible as it will be far off-resonance. We see from the $m_s = -1$ projection that the NV

experiences a field along S_z due to the ^{14}N spin projections in addition to the Rabi drive, as illustrated in 4.6.
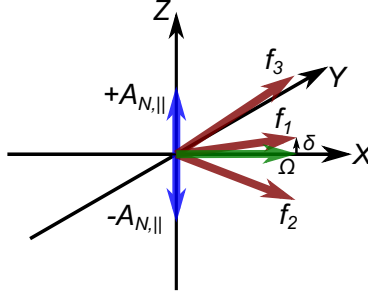

Figure 4.6: The NV will rotate about the vector sum, f_i, of the Rabi drive, Ω, the microwave detuning, δ, and the effective field provided by the ^{14}N, $\{0, \pm A_{N,\|}\}$.

These experiments were performed at room temperature and low field, thus the nitrogen spin state was effectively in the maximally mixed state, $\mathbf{1}/3$. In turn, the NV evolution due to the three ^{14}N spin projections will thus sum incoherently. Fitting the data with a phenomenological model for the referenced fluorescence signal, including an exponential decoherence effect:

$$F = \left(\sum_{i=1}^{3} A_i \cos(2\pi f_i t) \right) e^{-t/T_2} + C \tag{4.13}$$

we extract the Rabi drives reported above, see Table 4.2. With a Rabi drive of $\Omega = 4.38$ MHz (6.23 MHz in equation 4.5) and a detuning of $\delta = 0.5$ MHz we find that the resulting frequencies corresponding to the $m_{s,N} = 0$ spin projection (see Figure 4.6):

$$f_1 = \sqrt{\Omega^2 + \delta^2} = 4.408 \text{ MHz} \tag{4.14}$$

and for the $m_{s,N} = \pm 1$ spin projections:

$$f_{3,2} = f_{m_{s,N}=\pm 1} = \sqrt{\Omega^2 + (\pm A_{N,\|} + \delta)^2} \tag{4.15}$$

$$= \sqrt{f_1^2 + A_{N,\|}^2 \pm 2A_{N,\|}\delta} = \{5.20, 4.74\} \text{ MHz} \tag{4.16}$$

are in very good agreement with the fitted data.

For the high power Rabi signal the beating due to the nitrogen was not well resolved. Thus, only a single cosine was fit to the high power Rabi. The discrepancy between the decoherence times in the two experiments can be attributed to many possible sources, but

39

Parameter	Low Power Rabi	High Power Rabi
f_1 [MHz]	4.408 $\pm$0.038	
f_2 [MHz]	4.736 $\pm$0.006	13.02 $\pm$0.03
f_3 [MHz]	5.208 $\pm$0.004	
T_2 [μs]	9 $\pm$3	1.7 $\pm$0.5

Table 4.2: Phenomenological fits to the Rabi data presented in Figure 4.5b for low Rabi power, and Figure 4.5e for high Rabi power.

is most likely due to the varying proximity of the two NVs to the diamond surface [27].

The dark reference used during these experiments is performed using an Adiabatic Inversion pulse. To do this the phase of the control field is ramped quadratically, leading to a linearly changing phase slope:

$$\phi(t) = at^2 + b = \frac{\dot{\phi}t}{2} + b \tag{4.17a}$$

$$\dot{\phi} = 2at \tag{4.17b}$$

Letting $b = 0$, without loss of generality, we find the control Hamiltonian takes the form (the factor of $1/2$ being absorbed into $\dot{\phi}$):

$$H_c = \Omega \cos\left(\left(\omega + \dot{\phi}\right)t\right) S_x \tag{4.18}$$

To appreciate the effect of ramping the phase consider the case when $D = \omega + \dot{\phi}$, $\omega = \Delta - \gamma B_z$, and neglect nuclear hyperfine terms, then we have the effective Hamiltonian:

$$H_{eff} = \begin{pmatrix} 2\gamma B_z - \dot{\phi} & 0 & 0 \\ 0 & 0 & 0 \\ 0 & 0 & -\dot{\phi} \end{pmatrix} \tag{4.19}$$

Neglecting, as before, the off-resonant term arising from a large Zeeman splitting, we find that when $\dot{\phi} < 0$, the NV evolves under a Hamiltonian proportional to $+S_z^2$, whereas when $\dot{\phi} > 0$ the NV evolves under $-S_z^2$. If the phase slope is changed slowly compared to all energy gaps in the NV ground state, then the NV will evolve from the ground state of S_z^2 to $-S_z^2$ adiabatically [43], i.e. $m_s = -1$. This is precisely what is done to obtain the dark reference seen in Figure 4.5, the pulse is usually applied for between 1 and 2 μs which is $\gg 1/\Delta \approx 0.3$ ns.

Nuclear Spin	Hyperfine [MHz]
^{14}N	2.20 $\pm$0.02
^{13}C	13.69 $\pm$0.02
^{13}C	1.26 $\pm$0.02

Table 4.3: The hyperfine splittings extracted from Figure 4.8.

Ramsey Spectrum of NV Coupled to Two Carbons

Many experiments that we would like to perform with this instrument require that the NV be strongly coupled to nuclear spins in the diamond lattice. In diamonds grown from natural abundance carbon the occurrence of such NVs is rare. To find such an NV automated scripts have been written that search through a diamond sample with the confocal microscope. Whenever a fluorescent defect is identified by the image analysis software the instrument automatically runs a pre-programmed CW-ODMR experiment. For the moment, the user then manually browses the resulting CW spectra to find an NV of interest. During such a scan, a promising NV was found with at least one strongly coupled ^{13}C. To investigate further, Ramsey spectroscopy was performed on the NV.

In the Ramsey experiment the NV is put in a superposition with $\alpha = \beta = \sqrt{1/2}$ in equation 4.4 using a $\pi/2$ pulse calibrated from a prior Rabi Flop experiment. The NV is allowed to evolve under its internal Hamiltonian for a time τ and the NV is rotated back to a population with a second $\pi/2$ pulse, see Figure 4.7. Hyperfine terms in the Hamiltonian will rotate in the interaction frame defined by the ZFS, as in the Rabi case above. The resulting oscillations in the fluorescence are analysed to extract the Ramsey spectrum, see Figure 4.8. Fitting the resulting spectrum with Lorentzians with peak positions separated by three free parameters for the the nitrogen and two carbon hyperfine splittings the two carbons were identified, see Table 4.3.
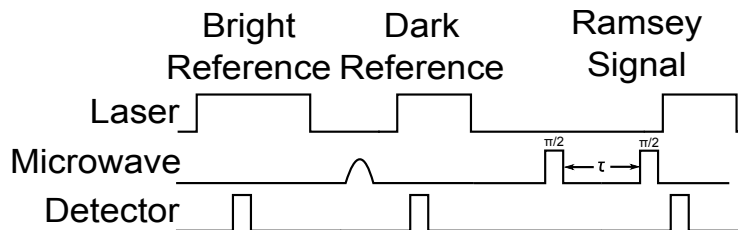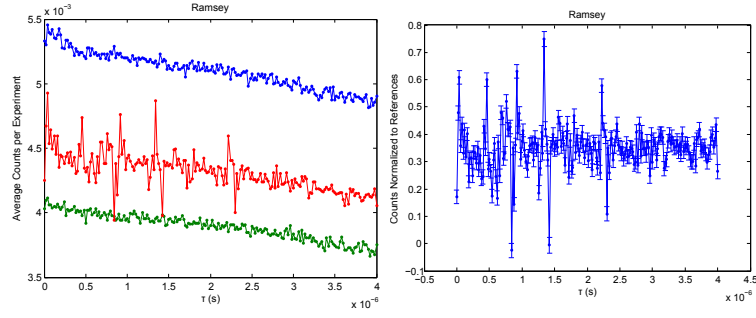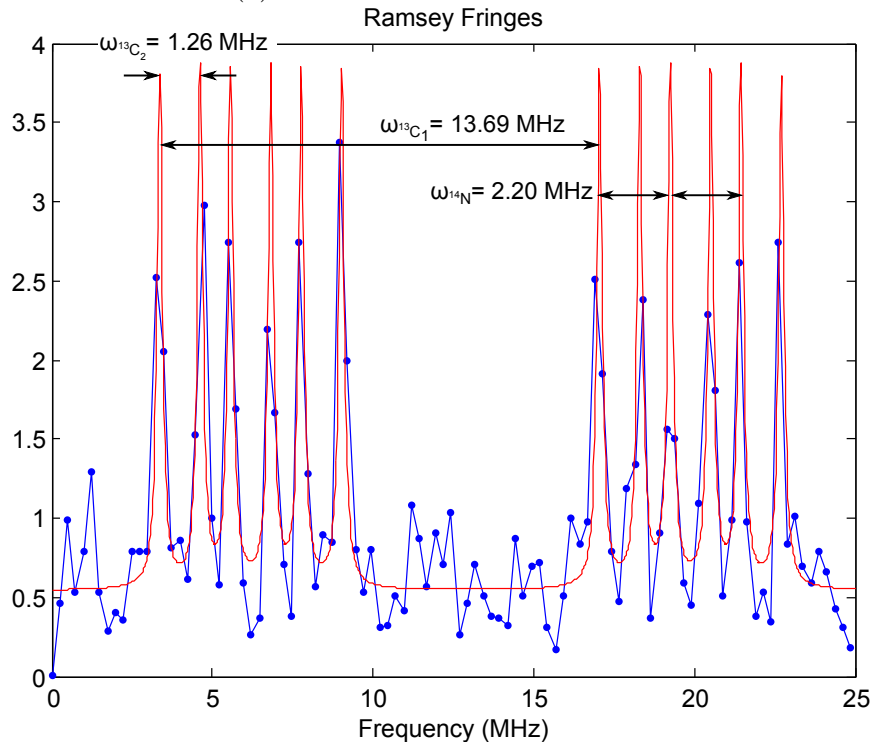

Figure 4.7: The pulse sequence for a Ramsey experiment. The time τ is swept.

(a)

(b)

(c)

Figure 4.8: a) The raw Ramsey time-domain signal with the bright and dark references shown. b) Data after being referenced, as in the Rabi case, see Figure 4.5. c) Fourier transform of the referenced data fit with 12 Lorentzians.

Chapter 5

Investigation Performed with the Instrument

The following presents an investigation performed with the instrument just described. This is work done with Dusan Sarenac, Ian Hincks, Osama Moussa, and, of course, David Cory. Importantly, Dusan performed the Halbach simulations and built the first prototype. The result will be submitted for publication shortly.

5.1 Dual Halbach Array for use in Nitrogen-Vacancy Centre Experiments

Nitrogen-Vacancy (NV) centres in diamond are fruitful systems for studying concepts of quantum information processing and quantum metrology. They exhibit long coherence times at room temperature and their spin state can be detected, initialized and polarized optically [40, 13, 14]. Single NV centres can be addressed and manipulated with confocal microscopy together with coherent microwave control [52]. The electronic ground state of the NV centre forms an effective spin-1 system, where the $m_s = 0$ and $m_s = \pm 1$ are separated by a zero field splitting $\Delta \approx 2.87$ GHz [53]. Further, a static external magnetic field can be applied to lift the degeneracy of the $m_s = \pm 1$ energy levels via the Zeeman interaction. The dynamics of the NV spin system depend on both the magnitude of the field as well as its alignment relative to the nitrogen-vacancy defect axis [73, 74]. In order to achieve high fidelity quantum control of the NV, an apparatus is required that can

apply a static magnetic field where both the magnitude and direction of the field can be controlled precisely.

In previous experiments, the static magnetic field has been applied using 3-axis Helmholtz coils [13] and single permanent magnets [74, 22]. The former solution leads to excessive thermal drift, while the latter is inconvenient for accessing a wide range of field magnitudes and angles. Our solution results in the thermal and mechanical stability provided by permanent magnets and the widely tunable field typically found with electromagnets.

The solution makes use of linear Halbach arrays, where each array is an arrangement of permanent magnets that enhances the magnetic field on one side of the array and minimizes the field on the other side [75, 76, 77]. The single sided nature of the field is achieved by varying the orientation of adjacent permanent magnets along the array, see Figure 5.1a. In the ideal case such an arrangement produces a constant magnitude magnetic field with varying direction on a line centred on and parallel to the array at a fixed height above the array. Note that due to the mirror symmetry of the array the magnetic field component perpendicular to the plane of symmetry is zero. Thus, at a point above the linear Halbach array, a constant magnitude magnetic field can be varied in polar orientation by sliding the Halbach array along its long axis.

Our design consists of stacking two linear Halbach arrays vertically, in such a way that the magnitude of the magnetic field produced by each array is equal at the confocal spot of the microscope, where the NV center would be located. The geometry is depicted in Figure 5.1b. To keep the magnitude constant and vary the angle of the field the arrays need to be moved simultaneously in the same direction. On the other hand if the two Halbach arrays are moved in opposition to each other then the angle of the magnetic field will remain constant while the magnitude varies. This is shown by the contour lines on Figure 5.2c and 5.2d. Such a design provides a wide range of field magnitudes over 360° in the xz-plane of the arrays. Rotating the two arrays up to 180° about the optical axis of the microscope provides access to one hemisphere of magnetic field vectors, see Figure 5.1c for the complete apparatus geometry. This is sufficient to either align or anti-align to all possible NV orientations in the diamond lattice.

In practice the finite dimensions of the magnets comprising the arrays and the finite extent of the arrays need to be considered to produce a reliable magnet system. Further, to access large magnitude magnetic fields we choose to keep the NV close to the Halbach arrays leading to further departures from the ideal case. To obtain a precise model of the expected field, a 3D Finite Element Model was computed for each of the two Halbach arrays in the commercial software COMSOL. The top array has six 1/4" x 1/4" x 1/16" magnet blocks, while the bottom has six 1/4" x 1/4" x 1/4" magnet blocks, all blocks have

a residual magnetization of $B_r = 1.32$ T. The dimensions of the magnet blocks composing the top array are chosen to be of the same x and y dimension as the cubes of the bottom array and smaller in z to produce a lower overall magnetic field to match that of the bottom array in the sample plane. The distance separating the two arrays was calculated based on the strength of the magnets and the relative location of the confocal spot. The sample plane in our resulting system is set to 7 mm above the top Halbach array and 10 mm above the bottom array.

The simulated components of the magnetic fields at the NV site as the arrays are moved along their long axes are presented in the top row of Figure 5.2. The simulation reproduces the null y-component of the magnetic fields resulting from the mirror symmetry of the arrays discussed above. The simulated magnetic field data can then be used to produce a map of magnetic field magnitudes and orientations that can be achieved with the independent motion of the arrays, as seen in the bottom row of Figures 5.2. These Figures show the magnitude and polar angle of the vectorial sum of the x- and z-components of the simulated field, illustrating the constant-magnitude and constant-angle contours.

The simulation shows that the x- and z-components of the Halbach arrays' magnetic fields do not have the same maximum value. This results in undulation in the magnitude of the total field. The maximum magnitude that can be oriented arbitrarily in one hemisphere is ≈ 600 G in our design, while the absolute maximum field is ≈ 750 G. This working area is depicted in Figures 2c) and 2d) by the bold rectangles. The expected uncertainty in magnitude and angle at a given dual Halbach array configuration is the gradient with respect to these coordinates times the repeatability of the linear actuators Δx, which in our case is 2μm,

$$\sigma_B(t,b) = \nabla |B| \cdot \Delta x \tag{5.1}$$

for relative uncertainty in magnitude, and

$$\sigma_\theta(t,b) = \nabla \theta \cdot \Delta x \tag{5.2}$$

for uncertainty in angle. We find the angle has a sharp gradient near zero-field as the dominant component of the magnetic field in this region changes sign, leading to an angle uncertainty up to $45°$. The working area excludes this region with a lower magnitude limit of 75 G yielding a maximum uncertainty of 0.4% in magnitude and $0.1°$ in polar angle. Dual Halbach arrays with stable regions at lower magnitudes can be designed by either increasing the distance from the arrays or initially building them with appropriately weaker magnets. Finally, by probing the raw field simulations 50 μm above and below the sample plane we find that the maximum field gradient in the z-direction is ≈ 0.12 G/μm.

A prototype of the dual Halbach array design was constructed and tested. Fast curing,

ultraviolet-activated epoxy (Dymax Corp.) was used to glue the permanent magnets (Nd-FeB, KJ Magnetics) to each other with the correct orientation and into a polycarbonate holder. The magnets were chosen to be commensurate with those simulated. Each polycarbonate holder was attached independently to a linear actuator with a position feedback system (Newport Corp.). This set-up was mounted on a rotation stage (Newport Corp.) where the rotation axis is co-axial with the optical axis of the confocal microscope objective. The dual Halbach apparatus was installed on a home-built scanning confocal microscope with a sample holder designed to accommodate the motion of the arrays while maintaining clearance between the polycarbonate casing and sample holder and the chosen distance between the top Halbach array and confocal spot, Figure 5.1c shows a schematic of the set-up.

Optically Detected Magnetic Resonance (ODMR) of single NVs is a good means of measuring the magnetic field at the confocal spot. The experiment consists of measuring a bright fluorescence reference with 30 ms of off-resonant optical excitation followed by application of low power microwave fields simultaneously with off-resonant optical excitation for 30 ms. The frequency of the microwaves is stepped and the procedure repeated. When the microwave frequency is resonant with the $m_s = 0 \rightarrow \pm 1$ transitions the NV fluorescence reduces and transitions are observed [40], see Figure 5.3a-c. To 0th-order the separation of the the resonances is given by:

$$\Delta\omega = 2\gamma_{NV}|\mathbf{B}|\cos(\theta) \tag{5.3}$$

where $\gamma_{NV} \approx 2.8$ MHz G^{-1}, $\mathbf{B}$ is the magnetic field vector, and θ is the angle between the magnetic field vector and the axis of symmetry of the NV centre.

To extract useful information from the NV, knowledge of its orientation in the diamond substrate is critical. To determine which of the four possible orientations an NV of interest was we measured ODMR spectra for a series of Halbach configurations with nearly constant magnetic field magnitude and changing angle in the xz-plane. We found configurations where $\Delta\omega \approx 0$, indicating that the field was nearly perpendicular to the NV axis. From the cut and orientation of the diamond substrate (Element Six) the NV was determined to be of either orientation 1 or 2, see Figure 5.1b.

To validate the Halbach prototype the fields produced by three Halbach configurations were probed with an NV: $\approx$50 G nearly parallel to the z-axis, $\approx$50 G tipped in the xz-plane, and $\approx$500 G also tipped in the xz plane, see Figure 5.3a-c. The measured Zeeman splittings and those predicted from the Halbach simulation were compared by computing contours from the simulation results shown in Figure 5.2 that would result in the measured splittings, see Figure 5.3d. The positions of the measured points are overlaid on the contours encircled

with circles of radius 300 μm, representing the experimental positional error of the arrays. This is greater than the actuator repeatability due to mechanical robustness issues. NV orientation 1 resulted in a dramatically poor fit, while for NV orientation 2 the data is seen to be in good agreement with the simulation, validating the prototype and the dual Halbach design. Greater mechanical robustness would lead to an improvement on our design and results.

We have demonstrated that our design provides reliable and accurate magnetic field control at a point above the arrays. This is specifically useful for NV center experiments as described. We note that the dual Halbach system could have wider applicability. Our design could find use in studies where the sample is small in spatial extent, high thermal and mechanical stability and field tunability is necessary, and clearance is required for the probe apparatus, such as studies with Scanning Probe Microscopes.
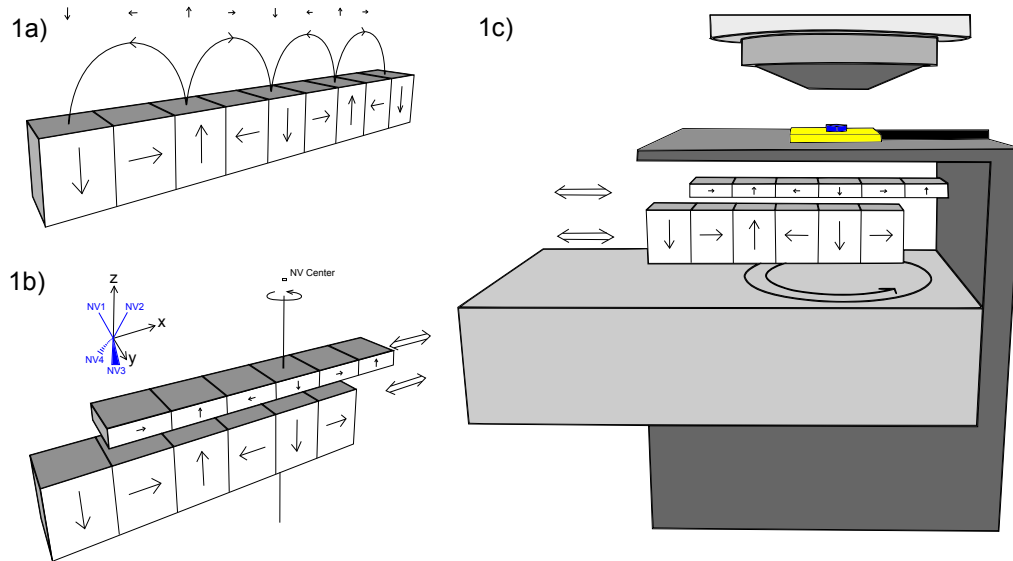
Figure 5.1: 1a) A single Halbach array composed of individual block magnets which vary in orientation to produce the depicted magnetic field above the array. 1b) Two stacked Halbach arrays which were designed to have an equal magnitude magnetic field at the NV center above. The degrees of motion which we control are indicated with the bidirectional arrows. The inset shows the potential NV orientations with respect to the axes defined for the Halbach system. 1c) The dual Halbach array placement in our confocal microscope. The bidirectional arrows represent the action of linear actuators.

47

Figure 5.2: Top Row) Simulated magnetic field strength at a fixed height above top array and above the bottom array. Bottom Row) Variation of the magnitude and angle of the ma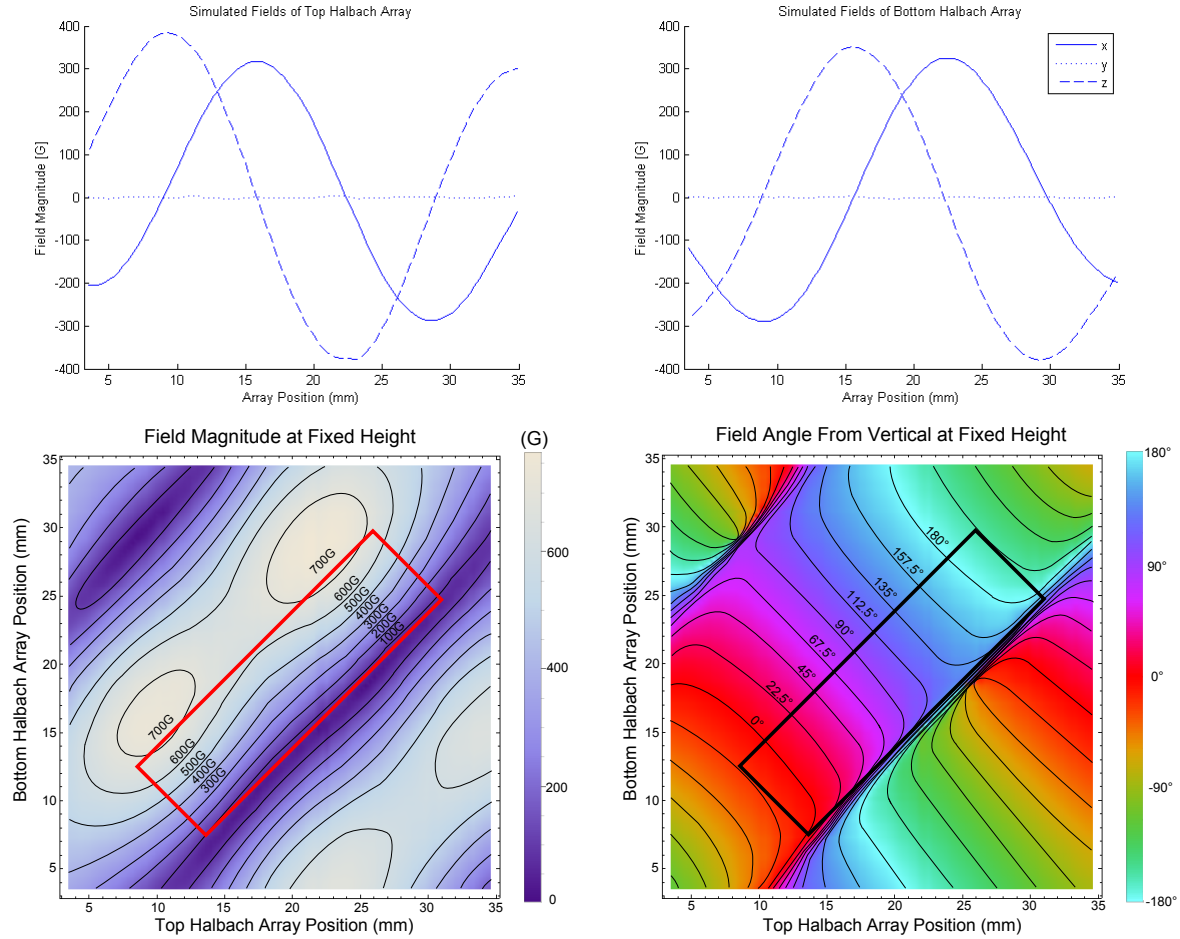gnetic field at a fixed point above the arrays with respect to the individual motion of the arrays. The working area is depicted by bold rectangles, which gives access to all magnitudes in one hemisphere with low uncertainty in magnitude and angle.
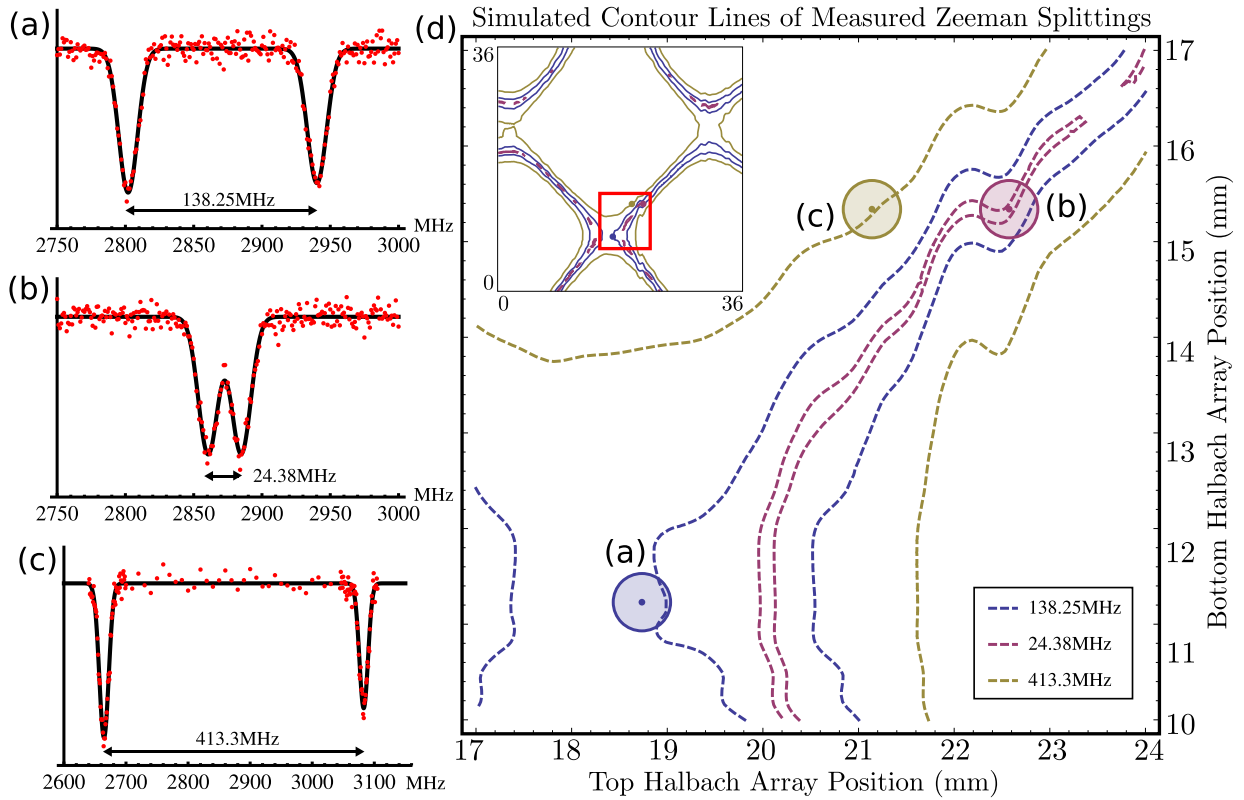
Figure 5.3: (a-c) ODMR fluorescence signal referenced to a bright reference for each data point. The resonance peak locations and, in turn, the projection of the magnetic field vector on the NV axis are extracted by fitting two Gaussian functions to the ODMR scans. The three scans correspond to the three points in part d. (d) Comparing the predicted transition separation to the measured separation. The contours trace the configurations at which to expect the measured splittings based on the magnetic field simulation and the knowledge of the NV orientation. The dots are placed at the actual Halbach array linear actuator values, where circles around the dots are of radius 300μm.

49

Chapter 6

Conclusion

When this project started, I was given an empty room and the task of building the instrument I have just presented. In this thesis I have detailed the workings of the confocal microscope and shown that it performs well as a microscope. Next I showed that the shaped microwave control built into the microscope can indeed be used to coherently manipulate Nitrogen-Vacancy centres in diamond. Rabi oscillations in the NV ground state were analysed and an NV with two nearby ^{13}C nuclear spins was observed using Ramsey spectroscopy. The value of the instrument was further demonstrated by investigating a dual Halbach array apparatus. Work can now begin in earnest to develop high-fidelity coherent control of NVs and to delve into the properties and uses of NVs.

6.1   Future Work

6.1.1   Measuring the Probability of $|m_s = 0\rangle$ Following Optical Pumping

An important property of the NV is that its electronic spin can be polarized optically, see Figure 2.1c. This property was used in previous chapters to produce initial states for the Rabi and Ramsey experiments as well as to provide a bright reference. Various attempts have been made to measure this polarization, however the reported values range from 42% to 96% [53].

We begin with defining the polarization concretely. The action of the laser on an NV

can be described with a refresh operator of the form:

$$R = \begin{pmatrix} \frac{1-p}{2} & 0 & 0 \\ 0 & p & 0 \\ 0 & 0 & \frac{1-p}{2} \end{pmatrix} \otimes \mathbf{Tr}_{NV}(\rho) \tag{6.1a}$$

$$= \begin{pmatrix} \frac{1-\epsilon}{3} & 0 & 0 \\ 0 & \frac{1+2\epsilon}{3} & 0 \\ 0 & 0 & \frac{1-\epsilon}{3} \end{pmatrix} \otimes \mathbf{Tr}_{NV}(\rho) \tag{6.1b}$$

where the operator acts on the space $\mathcal{H}_{NV} \otimes \mathcal{H}_{else}$, ρ is the NV system's density matrix, p is the probability of finding the NV in the $|m_s = 0\rangle$ state, $0 \le \epsilon \le 1$ is defined as the polarization of the NV, and $p = \frac{1+2\epsilon}{3}$.

To measure p precisely, we propose using a nearby ^{13}C as a resource, as shown in the quantum circuit in Figure 6.1a. This is work done in collaboration with Osama Mousa and Ian Hincks. The NV is first polarized by a refresh operation. The population of the NV thus polarized is swapped onto the nuclear spin. Finally, the NV is refreshed once again and the state of the carbon is read using Ramsey spectroscopy. Importantly, it is not necessary that the amount of polarization produced by the two refresh operations be identical. The heights of the ^{13}C Ramsey fringes will be dependant on the polarization of the carbon, see Figure 6.1b, which in turn was engineered to be dependant on the initial NV polarization. Indeed, under the secular approximation (*i.e.* neglecting terms that do not commute with S_z^2, the dominant component of the NV Hamiltonian), and assuming that the ^{14}N is projected into a single spin state, the ratio of ^{13}C peak heights, r, see Figure 6.1b, yields the following formula for p [78]:

$$p = \frac{A_{zz}^2(r-1) + 2A_{zx}^2 r}{A_{zz}^2(1-r) + 2A_{zx}^2(2+r)} \tag{6.2}$$

where A_{zz} and A_{zx} correspond to the carbon hyperfine tensor components corresponding to $S_z \otimes I_z$ and $S_z \otimes I_x$, respectively. We intend to implement the NV-C SWAP gate by using an Optimal Control Theory (OCT) derived microwave control sequence applied only on the NV and taking advantage of the anisotropy of the hyperfine tensor [11].

It is clear from equation 6.2 and the requirements of OCT that the carbon hyperfine tensor must be measured precisely in order to obtain a precise measurement of p. The approach we take is to measure the precession of the ^{13}C in the $m_s = 0$ manifold of the NV. When the external magnetic field is aligned to the NV principle axis, the Zeeman interaction sets the carbon's quantization axis. However, if the external field is not aligned to the NV axis then the ^{13}C precesses about a hyperfine-enhanced Zeeman axis [79]. The
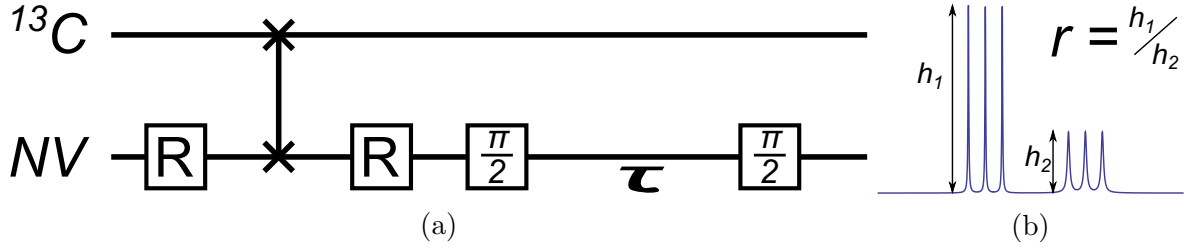
Figure 6.1: a) The quantum circuit for measuring the probability of finding the NV in the $|m_s = 0\rangle$ state after optical pumping. Figure adapted from [78] b) The expected form of the Ramsey spectrum from which p will be extracted, see equation 6.2.

measurement is performed by preparing the ^{13}C in an eigenstate of the $m_s = 1$ manifold using a selective π-pulse, see Figure 6.2a. Thus, the ^{13}C is left in a superposition of the $m_s = 0$ manifold eigenstates. This superposition is allowed to precess, and the state is finally probed with a second π-pulse.

We searched through many NVs to locate one with a ^{13}C that has a 12.8 MHz hyperfine interaction with the NV, which is expected to have a strong anisotropic hyperfine coupling to the NV [45]. Once found the orientation of the NV in the lab frame was determined by applying a number of magnetic fields with varying orientation and magnitude to the NV. Aligning the field and performing Ramsey spectroscopy revealed that we do indeed have a 12.8 MHz carbon. Finally, the experiment of Figure 6.2a was performed for a variety of magnetic field orientations with respect to the N-V axis, see Table 6.1 and Figure 6.2b-6.2d. A hyperfine tensor was fit to the resulting data yielding the following result:

$$\mathbf{A} = \begin{pmatrix} 16.8 & 0 & 2.03 \\ 0 & 12.8 & 0 \\ 2.03 & 0 & 12.6 \end{pmatrix} \tag{6.3}$$

where the values are in MHz. These values are commensurate with theoretical values found in literature [80]. Further, it is known that there are three locations in the lattice that a 12.8 MHz carbon can be found [45]. Another result from the fitting procedure was to determine which of these three possible carbons we have with the current NV. The problem is that when artificial noise of a few hertz is applied to the Larmor data the anisotropic component of the tensor varies by megahertz. To overcome this problem the experiment of Figure 6.2a should be simulated and the visibility of the Larmor data used in addition to the frequency to constrain the hyperfine tensor. Once the hyperfine tensor is determined precisely OCT pulses to measure p can be found and the measurement can be done.

Field $(|B|, \theta, \phi)$ [G,rad,rad]	Zeeman Splitting [MHz]	Enhanced Larmor [kHz]
$(36, \arccos(-1/3), 0)$	51.8	912.9
$(36, \arccos(-1/3), 2\pi/3)$	67.4	885.8
$(14, \pi/4, 0)$	54.0	271.3
$(14, \pi/4, \pi/6)$	54.3	313.2
$(14, \pi/4, 5\pi/3)$	55.5	264.6
$(14, 2\pi/3, 11\pi/6)$	41.0	296.7
$(10, 2\pi/3, 11\pi/6)$	29.3	211.7
$(10, \pi/3, \pi/3)$	28.1	263.6
$(14, 3\pi/8, \pi/7)$	28.6	390.6
$(14, 3\pi/8, -2\pi/7)$	29.8	336.6
$(14, 2\pi/3, -4\pi/13)$	39.1	329.1
$(14, \pi/4, -3\pi/20)$	54.4	245.8
$(14, \pi/4, -7\pi/20)$	55.3	267.3
$(14, \pi/4, -9\pi/40)$	54.7	247.3
$(14, \pi/4, -11\pi/40)$	54.9	253.4
$(14, 3\pi/8, -7\pi/40)$	71.5	133.0

Table 6.1: Enhanced Larmor precession of a 12.8 MHz ^{13}C measured via the NV for various magnetic field orientations with respect to the NV principle axis, where θ is the polar angle, and ϕ is the azimuthal angle with zero defined to be in the plane formed by the N-V vector and a vector connecting the NV to a nearest-neighbour carbon. The first two entries are approximately aligned to diamond bong directions. The Zeeman splittings are extracted from the CW-ODMR spectrum for the given field. The enhanced Larmor frequency is measured as described in the text.
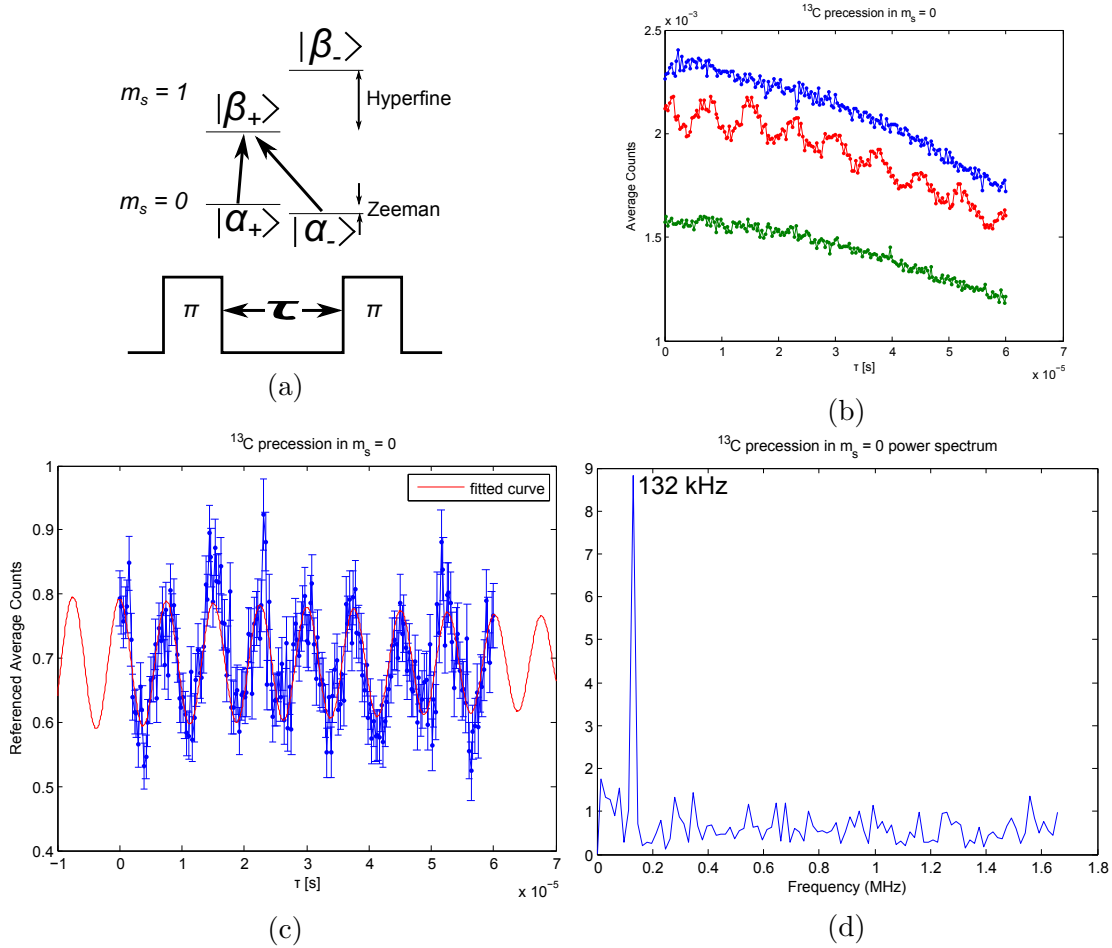
Figure 6.2: a) Selective π-pulses are used to produce an eignenstate of the ^{13}C in the $m_s = 1$ NV manifold and the precession in the manifold measured. The eiegenstates of the ^{13}C in the $m_s = 0, 1$ manifolds are represented by $|\alpha_\pm\rangle, |\beta_\pm\rangle$, respectively. b-d) Samle data showing enhanced Larmor precession of the ^{13}C in the $m_s = 0$: b) raw data, c) referenced data as in 4.5 fit with a cosine to extract the precession frequency, d) Fourier transform of referenced data.

6.1.2 Implementing Algorithmic Cooling on an NV and Nearby Nuclear Spins

Swapping the state of the refreshed NV onto the carbon in the above experiment polarizes the carbon nuclear spin, which is a useful state to prepare in quantum information

processing applications. Nuclear spin polarization via the NV has been demonstrated in the past at specific external magnetic fields [73] and with a SWAP gate [81]. A natural extension to swapping the polarized NV state onto the carbon is to use Algorithmic Cooling (AC) to enhance this initial polarization [82, 83]. The algorithm calls for at least two ancillary qubits one of which can be refreshed on demand, see Figure 6.3. The polarization of the target qubit is successively increased by 'compressing' the polarization of the refreshed qubit onto the target qubit. Since we are only concerned with populations in this algorithm the density matrix for the multi-qubit system is diagonal and we represent the density matrix with a column vector. The action of the compression steps for the first two rounds of AC starting with the maximally mixed state on a three qubits system is:

$$
\frac{1}{2^3}\begin{pmatrix}1\\1\\1\\1\\1\\1\\1\\1\end{pmatrix} \xrightarrow{R} \frac{1}{2^3}\begin{pmatrix}1+\epsilon\\1-\epsilon\\1+\epsilon\\1-\epsilon\\1+\epsilon\\1-\epsilon\\1+\epsilon\\1-\epsilon\end{pmatrix} \xrightarrow{AC_1} \frac{1}{2^3}\begin{pmatrix}1+\epsilon\\1+\epsilon\\1+\epsilon\\1+\epsilon\\1-\epsilon\\1-\epsilon\\1-\epsilon\\1-\epsilon\end{pmatrix} \xrightarrow{R} \frac{1}{2^3}\begin{pmatrix}(1+\epsilon)^2\\(1+\epsilon)(1-\epsilon)\\(1+\epsilon)^2\\(1+\epsilon)(1-\epsilon)\\(1+\epsilon)(1-\epsilon)\\(1-\epsilon)^2\\(1+\epsilon)(1-\epsilon)\\(1-\epsilon)^2\end{pmatrix} \xrightarrow{AC_2} \frac{1}{2^3}\begin{pmatrix}(1+\epsilon)^2\\(1+\epsilon)^2\\(1+\epsilon)(1-\epsilon)\\(1+\epsilon)(1-\epsilon)\\(1+\epsilon)(1-\epsilon)\\(1+\epsilon)(1-\epsilon)\\(1-\epsilon)^2\\(1-\epsilon)^2\end{pmatrix}
$$

$$(6.4)$$

where ϵ is the polarization of the refreshed qubit upon refreshing, and the qubit refresh operator, R, is:

$$
R = \frac{1}{2}\begin{pmatrix}1+\epsilon & 0\\ 0 & 1-\epsilon\end{pmatrix} \otimes \mathbf{Tr}_r\left(\rho_{tot}\right) \tag{6.5}
$$

As can be seen, the compression is achieved by sorting the system basis with respect to population. The theory indicates that if the amount of polarization on the refreshable qubit is greater than $1/2^n$, where n is the number of qubits being used, then a target qubit can be perfectly polarized [84].

The NV provides a convenient, room-temperature, refreshable qutrit. The ^{14}N spin-1 nuclear spin may be used as an ancillary qutrit, and, as before, the ^{13}C spin-$1/2$ nucleus remains the target qubit. With an expected polarization of the NV of $> 40\% > 1/2^3$ this system is expected to provide perfect polarization of the ^{13}C. Figure 6.4a shows the polarization achieved on the ^{13}C assuming the NV is polarized to $\epsilon = 92.5\%$, and the refresh operator is given by equation 6.1b. Also shown is a comparison to a system of three qubits where the refreshable qubit can be refreshed to $\epsilon = 92.5\%$, and the refresh operator is given by 6.5. The qutrit system is seen to be marginally better at polarizing the ^{13}C in the initial few steps than the all qubit system.
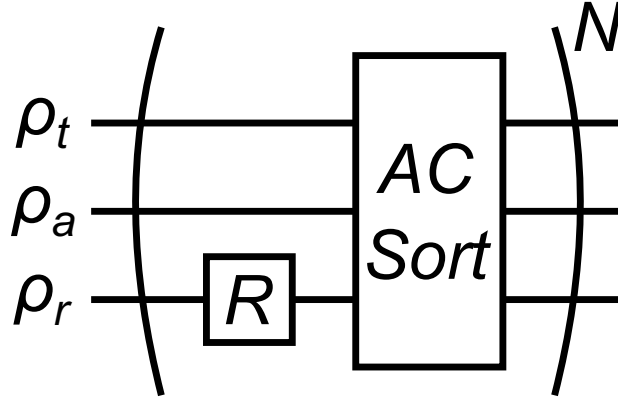
Figure 6.3: The quantum circuit for Algorithmic Cooling. Three quantum systems are represented with subscripts for 'refresh', ancilla', 'target'. In the two qutrit one qubit case, ρ_r is the NV qutrit, ρ_a is the ^{14}N qutrit, and ρ_t is the ^{13}C qubit.

However, if the gates in the quantum algorithm are not performed with perfect fidelity, then the final carbon polarization achievable is expected to be less. To simulate imperfect gates in the qutrit case, between each step of the algorithm a depolarizing channel was used:

$$\Lambda\left[\rho\right] = \left(1 - \text{err}\right)\rho + \text{err}\frac{\mathbf{1}}{18} \tag{6.6}$$

where the identity operator, $\mathbf{1}$, acts on the space $\mathcal{H}_{NV} \otimes \mathcal{H}_{^{14}N} \otimes \mathcal{H}_{^{13}C}$, ρ is the system density matrix, and err is the probability of depolarizing the system. The results are shown in Figure 6.4b. From these plots we see that to do better than a simple SWAP gate, given the refreshed NV's polarization is $\epsilon = 92.5\%$, a depolarizing probability of less than 5%, or fidelity of greater than 95%, is required.

A further issue with implementing AC on such a system is that the ^{14}N is difficult to control well using only microwave controls on the NV and the NV-^{14}N hyperfine interaction, as this interaction is nearly isotropic. Of course, this could be solved by using direct radio-frequency excitation of the nitrogen spin in conjunction with microwave control of the NV. An alternative is to use an NV with two nearby ^{13}C that have strongly anisotropic hyperfine tensors, such as the above 12.8 MHz carbon, or the nearest neighbour 130 MHz carbon. The likelihood of finding such an NV can be increased by growing diamond samples enriched with ^{13}C isotopes.
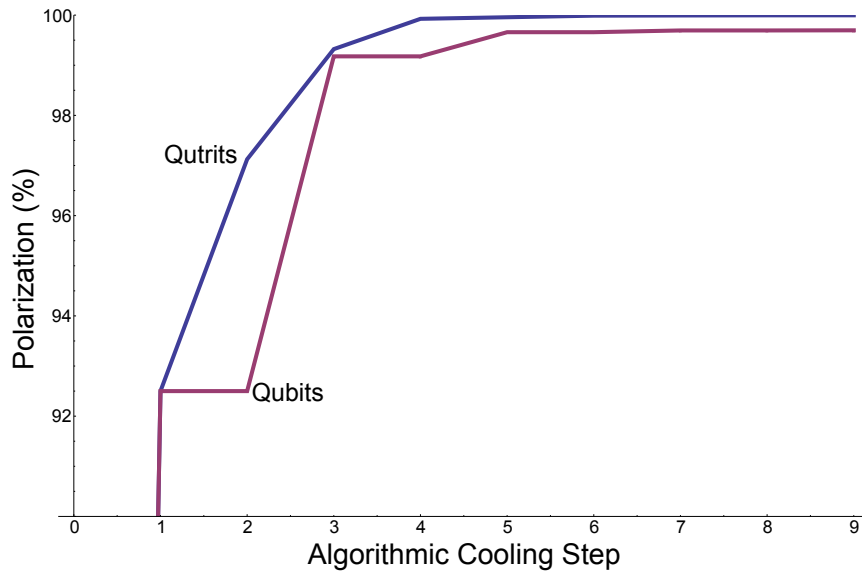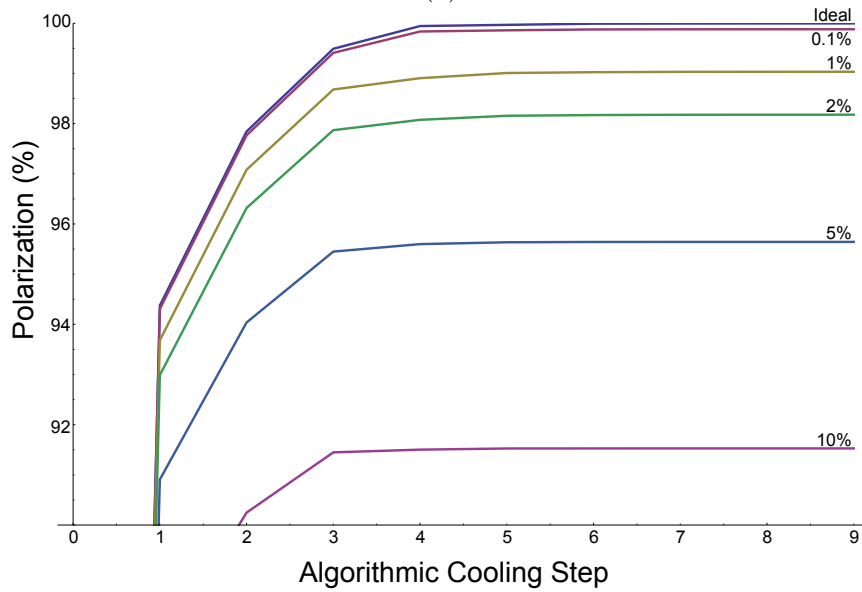
Figure 6.4: a) Comparing algorithmic cooling on a system of two qutrits and a qubit ('Qutrits') and three qubits ('Qubits'), with $\epsilon = 92.5\%$ in both cases. b) The effect of a depolarizing channel on achievable polarization on ^{13}C. The labels are the probability of depolarizing to the maximally mixed state, err in equation 6.6. I thank Chris Granade for helping implement the sorting function in *Mathematica*.

APPENDICES

Appendix A

Beam Tracing Calculator

The *Mathematica* code for the beam tracing calculator is presented below. I thank Chris Granade for helping me write this calculator.

airComponent = Function[$\{d, x, \theta, f\}, \{x + d * \theta, \theta\}$];

AirLensComponent = Function $\left[\{d, x, \theta, f\}, \left\{x * \left(1 - \frac{d}{f}\right) + d * \theta, \frac{-x}{f} + \theta\right\}\right]$;

testF2[new_, diverg_, d_, compList_]:=Module[{

$x = \{\text{new}\}$,

x2 = {0},

$\theta = \{0\}$,

$\theta 2 = \{\text{diverg}\}$,

Ray,

Ray2

},

{

(*Flat ray*)

Ray = Table[

{

$\text{compList}[[i, 2]][d - \text{compList}[[i, 1, 1]], x[[i]], \theta[[i]], \text{compList}[[i, 1, 3]]],$

$x =$

$x \sim \text{Join} \sim \{\text{compList}[[i, 2]][\text{compList}[[i, 1, 2]] - \text{compList}[[i, 1, 1]], x[[i]], \theta[[i]],$

$\text{compList}[[i, 1, 3]]][[1]]\},$

$\theta =$

$\theta \sim \text{Join} \sim \{\text{compList}[[i, 2]][\text{compList}[[i, 1, 2]] - \text{compList}[[i, 1, 1]], x[[i]], \theta[[i]],$

$\text{compList}[[i, 1, 3]]][[2]]\}$

$\}, \{i, 1, \text{Length}[\text{compList}]\}$

],

(*Angled ray*)

Ray2 = Table[

{

$\text{compList}[[i, 2]][d - \text{compList}[[i, 1, 1]], \text{x2}[[i]], \theta 2[[i]], \text{compList}[[i, 1, 3]]],$

x2 =

$\text{x2} \sim \text{Join} \sim \{\text{compList}[[i, 2]][\text{compList}[[i, 1, 2]] - \text{compList}[[i, 1, 1]], \text{x2}[[i]], \theta 2[[i]],$

$\text{compList}[[i, 1, 3]]][[1]]\},$

$\theta 2 =$

$\theta 2 \sim \text{Join} \sim \{\text{compList}[[i, 2]][\text{compList}[[i, 1, 2]] - \text{compList}[[i, 1, 1]], \text{x2}[[i]], \theta 2[[i]],$

$\text{compList}[[i, 1, 3]]][[2]]\}$

$\}, \{i, 1, \text{Length}[\text{compList}]\}$

],

(*Following is what we output to draw the beam profile;

the above was used for internal calculation and tracking*)

Apply[Which, Sequence@@@

Table[

{compList[[j, 1, 1]] $< d \le$ compList[[j, 1, 2]],

Sqrt [Ray[[j, 1, 1]]^2 + Ray2[[j, 1, 1]]^2] (*calcualtes the beam envelope from the two rays*)

}, {j, 1, Length[compList]}]

]}]

References

[1] R. P. Feynman. Simulating Physics with Computers. *Intl. J. of Theoretical Physics*, 21:467, 1982.

[2] P. Cappellaro, J. Emerson, N. Boulant, C. Ramanathan, S. Lloyd, and D. G. Cory. Entanglement Assisted Metrology. *Phys. Rev. Lett.*, 94:020502, Jan 2005.

[3] P. W. Shor. Polynomial-Time Algorithms for Prime Factorization and Discrete Logarithms on a Quantum Computer. *arXiv:quant-ph/9508027*, Jan 1996.

[4] Emanuel Knill, Raymond Laflamme, and Lorenza Viola. Theory of Quantum Error Correction for General Noise. *Phys. Rev. Lett.*, 84:2525–2528, Mar 2000.

[5] D. P. DiVincenzo. Topics in quantum computers. *arXiv:cond-mat/9612126*, Dec 1996.

[6] D. G. Cory, M. D. Price, W. Maas, E. Knill, R. Laflamme, W. H. Zurek, T. F. Havel, and S. S. Somaroo. Experimental Quantum Error Correction. *Phys. Rev. Lett.*, 81:2152–2155, Sep 1998.

[7] Osama Moussa, Jonathan Baugh, Colm A. Ryan, and Raymond Laflamme. Demonstration of Sufficient Control for Two Rounds of Quantum Error Correction in a Solid State Ensemble Quantum Information Processor. *Phys. Rev. Lett.*, 107:160501, Oct 2011.

[8] Y. Nakamura, Y. A. Pashkin, and J. S. Tsai. Coherent control of macroscopic quantum states in a single-Cooper-pair box. *Nature*, 398:786, Apr 1999.

[9] Hanhee Paik, D. I. Schuster, Lev S. Bishop, G. Kirchmair, G. Catelani, A. P. Sears, B. R. Johnson, M. J. Reagor, L. Frunzio, L. I. Glazman, S. M. Girvin, M. H. Devoret, and R. J. Schoelkopf. Observation of High Coherence in Josephson Junction Qubits Measured in a Three-Dimensional Circuit QED Architecture. *Phys. Rev. Lett.*, 107:240501, Dec 2011.

[10] J Baugh, J S Fung, J Mracek, and R R LaPierre. Building a spin quantum bit register using semiconductor nanowires. *Nanotechnology*, 21(13):134018, 2010.

[11] J. S. Hodges, J. C. Yang, C. Ramanathan, and D. G. Cory. Universal control of nuclear spins via anisotropic hyperfine interactions. *Phys. Rev. A*, 78:010303, Jul 2008.

[12] F. Jelezko, T. Gaebel, I. Popa, A. Gruber, and J. Wrachtrup. Observation of Coherent Oscillations in a Single Electron Spin. *Phys. Rev. Lett.*, 92:076401, Feb 2004.

[13] C. A. Ryan, J. S. Hodges, and D. G. Cory. Robust decoupling techniques to extend quantum coherence in diamond. *Phys. Rev. Lett.*, 105:200402, Nov 2010.

[14] G. Balasubramanian, P. Neumann, D. Twitchen, M. Markham, R. Kolesov, N. Mizuochi, J. Isoya, J. Achard, J. Beck, J. Tissler, V. Jacques, P. Hemmer, F. Jelezko, and J. Wrachtrup. Ultralong spin coherence time in isotopically engineered diamond. *Nature Materials*, 8:383, Apr 2009.

[15] N. Bar-Gill, L. M. Pham, A. Jarmola, D. Budker, and R. L. Walsworth. Solid-state electronic spin coherence time approaching one second. *Nature Comm.*, 4:1743, Nov 2012.

[16] L. Jiang, J. S. Hodges, J. R. Maze, P. Maurer, J. M. Taylor, D. G. Cory, P. R. Hemmer, R. L. Walsworth, A. Yacoby, A. S. Zibrov, and M. D. Lukin. Repetitive readout of a single electronic spin via quantum logic with nuclear spin ancillae. *Science*, 326(5950):267–272, 2009.

[17] P. C. Maurer, G. Kucsko, C. Latta, L. Jiang, N. Y. Yao, S. D. Bennett, F. Pastawski, D. Hunger, N. Chisholm, M. Markham, D. J. Twitchen, J. I. Cirac, and M. D. Lukin. Room-temperature quantum bit memory exceeding one second. *Science*, 336(6086):1283–1286, 2012.

[18] F. Dolde, I. Jakobi, B. Naydenov, N. Zhao, S. Pezzagna, C. Trautmann, J. Meijer, P. Neumann, F. Jelezko, and J. Wrachtrup. Room-temperature entanglement between single defect spins in diamond. *Nature Physics*, 9:139, Sep 2012.

[19] H. Bernien, B. Hensen, W. Pfaff, G. Koolstra, M. S. Blok, L. Robledo, T. H. Taminiau, M. Markham, D. J. Twitchen, L. Childress, and R. Hanson. Heralded entanglement between solid-state qubits separated by three metres. *Nature*, 497:86, May 2013.

[20] Bernhard Grotz, Johannes Beck, Philipp Neumann, Boris Naydenov, Rolf Reuter, Friedemann Reinhard, Fedor Jelezko, Jrg Wrachtrup, David Schweinfurth, Biprajit

Sarkar, and Philip Hemmer. Sensing external spins with nitrogen-vacancy diamond. *New Journal of Physics*, 13(5):055004, 2011.

[21] S. Steinert, F. Dolde, P. Neumann, A. Aird, B. Naydenov, G. Balasubramanian, F. Jelezko, and J. Wrachtrup. High sensitivity magnetic imaging using an array of spins in diamond. *Rev. Sci. Instrum.*, 81:043705, 2010.

[22] D. Le Sage, K. Arai, D. R. Glenn, S. J. DeVience, L. M. Pham, L. Rahn-Lee, M. D. Lukin, A. Yacoby, A. Komeili, and R. L. Walsworth. Optical magnetic imaging of living cells. *Nature*, 496:486, Apr 2013.

[23] G. Kucsko, P. C. Maurer, N. Y. Yao, M. Kubo, H. J. Noh, P. K. Lo, H. Park, and M. D. Lukin. Nanometer-scale thermometry in a living cell. *Nature*, 500:54, Aug 2013.

[24] Liam T. Hall, Charles D. Hill, Jared H. Cole, Brigitte Stdler, Frank Caruso, Paul Mulvaney, Jrg Wrachtrup, and Lloyd C. L. Hollenberg. Monitoring ion-channel function in real time through quantum decoherence. *Proceedings of the National Academy of Sciences*, 107(44):18777–18782, 2010.

[25] S. Steinert, F. Ziem, L. T. Hall, M. Zappe, A. Schweikert, N. Götz, A. Aird, G. Balasubramanian, L. Hollenberg, and J. Wrachtrup. Magnetic spin imaging under ambient conditions with sub-cellular resolution. *Nature Comm.*, 4:1607, Mar 2012.

[26] T. Staudacher, F. Ziem, L. Häussler, R. Stöhr, S. Steinert, F. Reinhard, J. Scharpf, A. Denisenko, and J. Wrachtrup. Enhancing the spin properties of shallow implanted nitrogen vacancy centers in diamond by epitaxial overgrowth. *Appl. Phys. Lett.*, 101:212401, Nov 2012.

[27] K. Ohno, Heremans. F. J., L. C. Bassett, B. A. Myers, D. M. Toyli, A. C. B. Jayich, C. J. Palmstrom, and D. D. Awschalom. Engineering shallow spins in diamond with nitrogen delta-doping. *Appl. Phys. Lett.*, 101:082413, Aug 2012.

[28] Birgit J M Hausmann, Thomas M Babinec, Jennifer T Choy, Jonathan S Hodges, Sungkun Hong, Irfan Bulu, Amir Yacoby, Mikhail D Lukin, and Marko Lonar. Single-color centers implanted in diamond nanostructures. *New Journal of Physics*, 13(4):045004, 2011.

[29] P. Maletinsky, S. Hong, M. S. Grinolds, B. Hausmann, M. D. Lukin, R. L. Walsworth, M. Loncar, and A. Yacoby. A robust scanning diamond sensor for nanoscale imaging with single nitrogen-vacancy centres. *Nature Nano.*, 7:320, Apr 2012.

[30] C. Wild and E. WÖrner. The CVD diamond booklet. Technical report, Diamond Materials GmbH.

[31] The British Monarchy. The Crown Jewels, August 2013. http://www.royal.gov.uk/.

[32] J. B. Hannay. On the Artificial Formation of the Diamond. *Proceedings of the Royal Society of London*, 30(200-205):450–461, 1879.

[33] F. P. Bundy, H. T. Hall, H. M. Strong, and R. H. Wentorf. Man-made diamonds. *Nature*, 176:51, Jul 1955.

[34] J. C. Angus, A. Argoitia, R. Gat, Z. Li, M. Sunkara, L. Wang, and Y. Wang. Chemical Vapour Deposition of Diamond. *Philosophical Transactions: Physical Sciences and Engineering*, 342(1664):195–208, 1993.

[35] Elment Six. Synthetic CVD Diamond eShop, August 2013. http://www.e6cvd.com/.

[36] P. Siyushev, H. Pinto, M. Vörös, A. Gali, F. Jelezko, and J. Wrachtrup. Optically controlled switching of the charge state of a single nitrogen-vacancy center in diamond at cryogenic temperatures. *Phys. Rev. Lett.*, 110:167402, Apr 2013.

[37] Yoshimi Mita. Change of absorption spectra in type-i b diamond with heavy neutron irradiation. *Phys. Rev. B*, 53:11360–11364, May 1996.

[38] NIMSoffice. Wikipedia: Nitrogen-Vacancy Centre, December 2008. http://commons.wikimedia.org/wiki/File:NV.JPG.

[39] N. B. Manson, J. P. Harrison, and M. J. Sellars. Nitrogen-vacancy center in diamond: Model of the electronic structure and associated dynamics. *Phys. Rev. B*, 74:104303, Sep 2006.

[40] F Jelezko and J Wrachtrup. Read-out of single spins by optical spectroscopy. *Journal of Physics: Condensed Matter*, 16(30):R1089, 2004.

[41] J. A. Weil and J. R. Bolton. *Electron Paramagnetic Resonance*. Wiley, 2nd edition, 2007.

[42] S. Felton, A. M. Edmonds, M. E. Newton, P. M. Martineau, D. Fisher, D. J. Twitchen, and J. M. Baker. Hyperfine interaction in the ground state of the negatively charged nitrogen vacancy center in diamond. *Phys. Rev. B*, 79:075203, Feb 2009.

[43] D. J. Griffiths. *Introduction to Quantum Mechanics*. Prentice Hall, 2nd edition, 2005.

[44] Xing-Fei He, Neil B. Manson, and Peter T. H. Fisk. Paramagnetic resonance of photoexcited n- V defects in diamond. ii. hyperfine interaction with the ^{14}N nucleus. *Phys. Rev. B*, 47:8816–8822, Apr 1993.

[45] Benjamin Smeltzer, Lilian Childress, and Adam Gali. ^{13}C hyperfine interactions in the nitrogen-vacancy centre in diamond. *New Journal of Physics*, 13(2):025021, 2011.

[46] A. Dréau, J.-R. Maze, M. Lesik, J.-F. Roch, and V. Jacques. High-resolution spectroscopy of single NV defects coupled with nearby ^{13}C nuclear spins in diamond. *Phys. Rev. B*, 85:134107, Apr 2012.

[47] T. H. Taminiau, J. J. T. Wagenaar, T. van der Sar, F. Jelezko, V. V. Dobrovitski, and R. Hanson. Detection and control of individual nuclear spins using a weakly coupled electron spin. *Phys. Rev. Lett.*, 109:137602, Sep 2012.

[48] L J Rogers, S Armstrong, M J Sellars, and N B Manson. Infrared emission of the NV centre in diamond: Zeeman and uniaxial stress studies. *New Journal of Physics*, 10(10):103024, 2008.

[49] A. Batalov, V. Jacques, F. Kaiser, P. Siyushev, P. Neumann, L. J. Rogers, R. L. McMurtrie, N. B. Manson, F. Jelezko, and J. Wrachtrup. Low Temperature Studies of the Excited-State Structure of Negatively Charged Nitrogen-Vacancy Color Centers in Diamond. *Phys. Rev. Lett.*, 102:195506, May 2009.

[50] G. D. Fuchs, V. V. Dobrovitski, R. Hanson, A. Batra, C. D. Weis, T. Schenkel, and D. D. Awschalom. Excited-state spectroscopy using single spin manipulation in diamond. *Phys. Rev. Lett.*, 101:117601, Sep 2008.

[51] F. Jelezko, I. Popa, A. Gruber, C. Tietz, J. Wrachtrup, A. Nizovtsev, and S. Kilin. Single spin states in a defect center resolved by optical spectroscopy. *Appl. Phys. Lett.*, 81:2160, Sep 2002.

[52] A. Gruber, A. Drbenstedt, C. Tietz, L. Fleury, J. Wrachtrup, and C. von Borczyskowski. Scanning confocal optical microscopy and magnetic resonance on single defect centers. *Science*, 276(5321):2012–2014, 1997.

[53] Marcus W. Doherty, Neil B. Manson, Paul Delaney, Fedor Jelezko, Jrg Wrachtrup, and Lloyd C.L. Hollenberg. The nitrogen-vacancy colour centre in diamond. *Physics Reports*, 528(1):1 – 45, 2013.

[54] E. Hecht. *Optics*. Addison Wesley, 4th edition, 2002.

[55] M. Minsky. Microscopy apparatus. Patent. US 3,013,467. Dec 1961.

[56] M. Minsky. Memoir on Inventing the Confocal Microscope. *Scanning*, 10:128–138, 1988.

[57] H. Kogelnik and T. Li. Laser Beams and Resonators. *Applied Optics*, 5(10):1550, Oct 1966.

[58] M. Born and E. Wolf. *Principles of Optics*. Cambridge University Press, 7th edition, 2001.

[59] J. Arnaud. Representation of Gaussian beams by complex rays. *Applied Optics*, 24(4):538, Feb 1985.

[60] Thorlabs Inc., August 2013. http://www.thorlabs.com/.

[61] 1250C-484 Acouso-Optic Modulator Datasheet. Isomet Corp.

[62] P. S. Tsai, N. Nishimura, E. J. Yoder, E. M. Dolnick, G. A. White, and D. Kleinfeld. Principles, Design, and Construction of a Two-Photon Laser-Scanning Microscope for *In Vitro* and *In Vivo* Brain Imaging. In R. D. Frostig, editor, *In Vivo Optical Imaging of Brain Function*. CRC Press, 2002.

[63] R. Herloski, S. Marshal, and R. Antos. Gaussian beam ray-equivalent modeling and optical design. *Applied Optics*, 22(8):1168, Apr 1983.

[64] Nikon Instruments Inc. Microscope Components for Transmitted Light Applications, Jan 2001.

[65] Nikon Instruments Inc. Tube Lens CFI 60 Drawing, 2012. Recieved in personal communication with Edward Lieser of Nikon.

[66] Semrock, Inc., August 2013. http://www.semrock.com/.

[67] 1951 USAF resolution test chart, August 2013. http://en.wikipedia.org/wiki/1951_USAF_resolution_test_chart.

[68] Robert H Webb. Confocal optical microscopy. *Reports on Progress in Physics*, 59(3):427, 1996.

[69] 2013. Personal communication with Roman Yasinsky of Isomet Corp.

[70] C. P. Slichter. *Principles of Magnetic Resonance*. Springer-Verlag, 3rd edition, 1990.

[71] C. Ryan. NV Interaction Frame Calculation. *Unpublished*, 2010.

[72] These calculations were made much easier with the in-house *Mathematica* packages *QuantumUtils*, written primarily by Chris Wood, Chris Granade, and Ian Hincks, and *NVSim*, written primarily by Ian Hincks.

[73] V. Jacques, P. Neumann, J. Beck, M. Markham, D. Twitchen, J. Meijer, F. Kaiser, G. Balasubramanian, F. Jelezko, and J. Wrachtrup. Dynamic Polarization of Single Nuclear Spins by Optical Pumping of Nitrogen-Vacancy Color Centers in Diamond at Room Temperature. *Phys. Rev. Lett.*, 102:057403, Feb 2009.

[74] J. H. Shim, B. Nowak, I. Niemeyer, J. Zhang, F. D. Brandao, and D. Suter. Characterization of hyperfine interaction between single electron and single nuclear spins in diamond assisted by quantum beat from the nuclear spin. *arXiv:1307.0257*, 2013.

[75] W. K. Westmijze. Permanent magnet. Patent. US 2,981,871. 1961.

[76] J. C. Mallinson. One-Sided Fluxes - A Magnetic Curiosity? *IEEE Transactions on Magnetics*, 9:679, 1973.

[77] K. Halbach. Design of Permanent Multipole Magnets with Orientated Rare Earth Cobalt Material. *Nuclear Instruments and Methods*, 169, 1980.

[78] I. Hincks. P_0 Experiment Analysis. *Unpublished Mathematica Notebook*, 2013.

[79] J. S. Hodges. Nitrogen-Vacancy Secular Hamiltonian Calculation. *Unpublished*, 2008.

[80] Adam Gali, Maria Fyta, and Efthimios Kaxiras. *Ab initio* supercell calculations on nitrogen-vacancy center in diamond: Electronic structure and hyperfine tensors. *Phys. Rev. B*, 77:155206, Apr 2008.

[81] M. V. Gurudev Dutt, L. Childress, L. Jiang, E. Togan, J. Maze, F. Jelezko, A. S. Zibrov, P. R. Hemmer, and M. D. Lukin. Quantum register based on individual electronic and nuclear spin qubits in diamond. *Science*, 316(5829):1312–1316, 2007.

[82] Leonard J. Schulman and Umesh V. Vazirani. Molecular scale heat engines and scalable quantum computation. In *IN 31ST STOC*, pages 322–329, 1999.

[83] J. Baugh, O. Moussa, C. A. Ryan, A. Nayak, and R. Laflamme. Experimental implementation of heat-bath algorithmic cooling using solid-state nuclear magnetic resonance. *Nature*, 438:470.

[84] L. J. Schulman, T. Mor, and Y. Weinstein. Physical limits of heat-bath Algorithmic Cooling. *SIAM J. Computing*, 36:1729–1747.